A&A 551, A8 (2013)
DOI: 10.1051/0004-6361/201220389

Astronomy & Astrophysics

Distant galaxy clusters in a deep *XMM-Newton* field within the CFTHLS D4⋆,⋆⋆,⋆⋆⋆

A. de Hoon[1], G. Lamer[1], A. Schwope[1], M. Mühlegger[2], R. Fassbender[2], H. Böhringer[2], M. Lerchster[2], A. Nastasi[2], R. Šuhada[6], M. Verdugo[2,7], J. P. Dietrich[6], F. Brimioulle[6], P. Rosati[2], D. Pierini⋆⋆⋆⋆, J. S. Santos[3], H. Quintana[4], A. Rabitz[1], and A. Takey[1,5]

[1] Leibniz-Institut für Astrophysik Potsdam (AIP), An der Sternwarte 16, 14482 Potsdam, Germany
e-mail: arjen@aip.de
[2] Max-Planck-Institut für extraterrestische Physik, Giessenbachstraße, 85748 Garching, Germany
[3] European Space Astronomy Center (ESAC)/ESA, Madrid, Spain
[4] Departamento de Astronomá y Astrofísica, Pontificia Universidad Católica de Chile, Casilla 306, 22 Santiago, Chile
[5] National Research Institute of Astronomy and Geophysics (NRIAG), Helwan, Cairo, Egypt
[6] University Observatory Munich, Ludwig-Maximillians University Munich, Scheinerstr. 1, 81679 Munich, Germany
[7] Institut für Astronomie, Universität Wien, Universitätsring 1, 1010 Wien, Austria

Received 15 September 2012 / Accepted 6 December 2012

ABSTRACT

Aims. The *XMM-Newton* distant cluster project (XDCP) aims at the identification of a well defined sample of X-ray selected clusters of galaxies at redshifts $z \geq 0.8$. As part of this project, we analyse the deep *XMM-Newton* exposure covering one of the CFHTLS deep fields to quantify the cluster content. We validate the optical follow-up strategy as well as the X-ray selection function.
Methods. We searched for extended X-ray sources in archival *XMM-Newton* EPIC observations. Multi-band optical imaging was performed to select high redshift cluster candidates among the extended X-ray sources. Here we present a catalogue of the extended sources in one the deepest ~250 ks *XMM-Newton* fields targetting LBQS 2212-1759 covering ~0.2 deg^2. The cluster identification is based on deep imaging with the ESO VLT and from the CFHT legacy survey, among others. The confirmation of cluster candidates is done by VLT/FORS2 multi-object spectroscopy. Photometric redshifts from the CFHTLS D4 were utilised to confirm the effectiveness of the X-ray cluster selection method. The survey sensitivity was computed with extensive Monte-Carlo simulations.
Results. At a flux limit of $S_{0.5-2.0\,\mathrm{keV}} \sim 2.5 \times 10^{-15}$ erg s^{-1} we achieve a completeness level higher than 50% in an area of ~0.13 deg^2. We detect six galaxy clusters above this limit with optical counterparts, of which 5 are new spectroscopic discoveries. Two newly discovered X-ray luminous galaxy clusters are at $z \geq 1.0$, another two at $z = 0.41$, and one at $z = 0.34$. For the most distant X-ray selected cluster in this field at $z = 1.45$, we find additional (active) member galaxies from both X-ray and spectroscopic data. Additionally, we find evidence of large-scale structures at moderate redshifts of $z = 0.41$ and $z = 0.34$.
Conclusions. The quest for distant clusters in archival *XMM-Newton* data has led to detection of six clusters in a single field, making *XMM-Newton* an outstanding tool for cluster surveys. Three of these clusters are at $z \geq 1$, which emphasises the valuable contribution of small, yet deep surveys to cosmology. Beta models are appropriate descriptions of the cluster surface brightness when performing cluster detection simulations to compute the X-ray selection function. The constructed $\log N - \log S$ tends to favour a scenario where no evolution in the cluster X-ray luminosity function (XLF) takes place.

Key words. cosmology: observations – dark matter – large-scale structure of Universe – X-rays: galaxies: clusters – surveys

1. Introduction

Clusters of galaxies are the largest gravitationally bound objects in the Universe and are tracers of the cosmic structure. Since their formation and evolution depends sensitively on the cosmological parameters, they are strong cosmological probes. Identification of clusters from X-ray surveys is currently the best method of constructing well defined samples of galaxy clusters for cosmological studies. The X-ray emission of the intracluster gas depends mostly on the square of the gas density. Owing to the peaked gas density distribution of clusters, the X-ray emission is more compact than the distribution of cluster galaxies, hence less affected by projection effects. For these reasons the X-ray luminosity is a good proxy of the total cluster mass.

The identification of ROSAT X-ray sources has resulted in large samples of local clusters (e.g. Böhringer et al. 2004, REFLEX) and a limited number of clusters at intermediate redshifts $z > 0.4$ (e.g. Vikhlinin et al. 1998). Only five distant clusters beyond $z = 1$ have been found among the ROSAT sources, most of them in the ROSAT Deep Cluster Survey (Rosati et al. 1998, RDCS).

Among the large number of extended sources serendipitously detected by *XMM-Newton* (Schwope et al. 2004; Lloyd-Davies et al. 2011; Takey et al. 2011) one can expect a significant fraction of distant clusters of galaxies. To date, about

⋆ This work made use of observations made with ESO Very Large Telescope at the La Silla Observatory under the programmes 072.A-0706(A), 073.A-0737(A), 079.A-0369(C), and 080.A-0659(A).
⋆⋆ *XMM-Newton*, an ESA science mission with instruments and contributions directly funded by ESA Member States and NASA.
⋆⋆⋆ Tables 2 and 5 are only available at the CDS via anonymous ftp to cdsarc.u-strasbg.fr (130.79.128.5) or via http://cdsarc.u-strasbg.fr/viz-bin/qcat?J/A+A/551/A8
⋆⋆⋆⋆ Freelance astronomer.

40 clusters beyond redshift $z \gtrsim 1$ and about 10 $z \gtrsim 1.4$ are known, of which IDCS J1426.5+3508 at $z = 1.75$ (Stanford et al. 2012), ClG J0218.3-0510 at $z = 1.62$ (Papovich et al. 2010; Tanaka et al. 2010; Pierre et al. 2012), XMMU J0338.8+0021 at $z = 1.49$ (Nastasi et al. 2011), LH146 at $z = 1.75$ (Henry et al. 2010), XMMU J0044.0-2033 at $z = 1.58$ (Santos et al. 2011), and XMMU J1007.4+1237 at $z = 1.56$ (Fassbender et al. 2011b) are the most distant ones. There have also been claims of even more distant clusters at $z \sim 2$ (Andreon et al. 2009; Gobat et al. 2011); however, these sources lack either a clear X-ray detection or spectroscopic confirmation.

We are conducting a focussed project on the identification of distant ($z \geq 0.8$) clusters from serendipitously detected *XMM-Newton* sources, the *XMM-Newton* distant cluster project (XDCP, Böhringer et al. 2005; Lamer et al. 2006; Fassbender et al. 2011a). An early success was our discovery of the most distant cluster of that time, XMMU 2235.3-2557 at $z = 1.39$ (Mullis et al. 2005). To date, the XDCP has been contributing half of the known sample of distant galaxy clusters. The sample contains 22 X-ray bright sources in the redshift range $0.9 < z < 1.6$ alone (Fassbender et al. 2011a).

In the current paper we report on the extended X-ray sources found in the field of the broad absorption line (BAL) QSO LBQS 2212-1759. This object has been repeatedly targetted with *XMM-Newton*, so that the field features one of the deepest *XMM-Newton* EPIC (European Photon Imaging Camera) exposures taken at that point. This field also received deep optical imaging coverage by the ESO Imaging Survey (EIS field XMM-07, Dietrich et al. 2006; Mignano et al. 2007) and the Canada-France-Hawaii Telescope (CFHT) legacy survey (LS) deep field four (D4). Furthermore, we have performed extensive spectroscopic follow-up with VLT/FORS2 to confirm cluster membership. We supply a complete X-ray source list of the stacked X-ray images for point sources in Table 2 (available at the CDS). However, in this paper, we focus on the content of only extended sources (Table 3).

The paper is structured as follows. In Sect. 2 we describe the X-ray source detection and the X-ray spectral analysis of the brightest extended sources. Section 3 gives an overview of the optical data available for the field and describes the galaxies over-densities in photometric redshift space derived from them. The spectroscopic confirmation of the cluster candidates is presented next in Sect. 4. Section 5 presents the optical identifications of the extended X-ray sources and the cluster redshifts. In the same section, the identification of the individual objects is discussed. The cosmological interpretation of our results is finally presented in Sect. 6.

We adopt a cosmology of $H_0 = 70\,\mathrm{km\,s^{-1}\,Mpc^{-1}}$, $\Omega_M = 0.3$, and $\Omega_\Lambda = 0.7$ and magnitudes are in the AB system.

2. *XMM-Newton* observations

2.1. X-ray data reduction and source detection

XMM-Newton has repeatedly targetted (yet never detected) the BAL QSO LBQS 2212-1759 (Clavel et al. 2006). The field received a total good exposure of 250 ks and is thus one of the deepest XMM fields. We retrieved the EPIC data sets from the public XMM archive (XSA) and processed the data from observation data files (ODFs) with the XMM science analysis software (`XMM-SAS v. 6.5`)[1]. Source detection runs with one of the latest versions `XMM-SAS v. 11` show no major changes with respect to the source list used in this work. We therefore remain with the older version for consistency and comparison with the 2XMM catalogue.

Table 1. Summary of *XMM-Newton* observations.

ObsID	Date	Good exposure time[s]		
		MOS1	MOS2	PN
0106660101	2000-11-17	57 229	57 273	54 829
0106660201	2000-11-18	52 177	52 073	38 247
0106660401	2001-11-16	33 350	33 561	–
0106660501	2001-11-17	8063	8091	5665
0106660601	2001-11-17	100 790	101 211	84 178
total		251 609	252 209	182 919

To screen the data for periods of high particle background, we created light curves of the high energy (7–15 keV) events for each of the three EPIC cameras. Periods where the count rate was more than 30% higher than the median rate were excluded from the later analysis. Table 1 shows the remaining exposure times of cleaned data for the individual pointing.

The event lists of each observation were transformed to a common astrometric frame (using the `XMM-SAS` task `attcalc`) and images in the five standard *XMM-Newton* energy bands (Watson et al. (2009), *band 1*: 0.2–0.5 keV, *band 2*: 0.5–1.0 keV, *band 3*: 1.0–2.0 keV, *band 4*: 2.0–4.5 keV, *band 5*: 4.5–12.0 keV) were binned for each camera and exposure. These bands differ from the energy bands (with a focus on 0.35–2.4 keV) usually used within the XDCP collaboration (Fassbender et al. 2011a).

For each of these images, an exposure map, background map, and detection mask were created using the respective `XMM-SAS` source detection tasks. Subsequently, the science images, exposure maps, and background maps of the individual exposures were added, creating one image for each of the three cameras and five energy bands.

In the softest band (0.2–0.5 keV) some of the EPIC detectors show spatially and temporally variable background features that can lead to spurious detections of extended sources. On the other hand, the thermal spectra of galaxy clusters only have a small fraction of their count rates in the hardest band beyond 4.5 keV. Therefore we restricted the detection of extended sources to the energy bands 2–4.

Source detection with the `XMM-SAS` tasks `eboxdetect` and `emldetect` was performed simultaneously on the nine images from three cameras and three energy bands. The task `eboxdetect` applies a sliding box detection algorithm to the input images. The resulting list is passed to the task `emldetect`, which fits the calibration PSF, optionally convolved with an extent model, to each input source. Extended sources were modelled using a King profile of the form

$$f(x,y) = \left(1 + \frac{(x-x_0)^2 + (y-y_0)^2}{r_c^2}\right)^{-3/2} \quad (1)$$

with core radii between $r_c = [4.0'' - 80.0'']$ as the model's extent parameter space. $x - x_0$ and $y - y_0$ are pixel coordinates relative to the central pixel of the object considered. The thresholds for the detection likelihoods were set to $L = 5.0$ for `eboxdetect` and $L = 6.0$ for `emldetect`, with $L = -\ln(P_{\mathrm{false}})$. This corresponds to probabilities of false detection of $P = 6.7 \times 10^{-3}$ and $P = 2.5 \times 10^{-3}$.

[1] XMM-SAS version 6.5 was the prototypical release used to construct the 2XMM catalogue (Watson et al. 2009).

Table 3. Extended X-ray sources properties from source detection.

Seq. #	Source XMMU J..	CTS	$CR_{0.5-4.5\,keV}$ 10^{-3} s^{-1}	$S_{0.5-2.0\,keV}$ 10^{-15} erg cm^{-2} s^{-1}	r_c arcsec	EXT_LIKE	DET_LIKE
1	221536.8–174534	7982	42.3 ± 1.00	36.3 ± 0.9	17.8 ± 0.5	696.6	2278.7
2	221558.6–173810	1807	17.3 ± 0.70	13.3 ± 0.6	10.8 ± 0.6	154.0	580.4
3	221500.9–175038	1055	9.19 ± 0.91	8.65 ± 0.73	25.9 ± 2.1	42.2	80.5
4	221557.5–174029	909	8.79 ± 0.65	7.26 ± 0.53	14.9 ± 1.1	61.7	136.8
5	221556.6–175139	689	6.55 ± 0.71	5.69 ± 0.58	16.8 ± 1.8	26.3	61.6
6	221503.6–175215	485	4.75 ± 0.74	3.76 ± 0.62	19.4 ± 3.0	7.3	21.3
7	221546.2–174002	384	2.66 ± 0.36	1.88 ± 0.29	10.5 ± 1.7	6.6	24.8
8	221551.7–173918	384	3.32 ± 0.41	1.98 ± 0.32	9.3 ± 1.5	8.1	35.0
9	221624.3–173321	380	24.6 ± 3.60	29.9 ± 4.3	20.1 ± 3.9	19.7	64.4

Notes. CTS stands for photon counts, CR for count rate, S for flux, EXT_LIKE is the extent likelihood, and DET_LIKE the detection likelihood. The core radius is denoted by r_c.

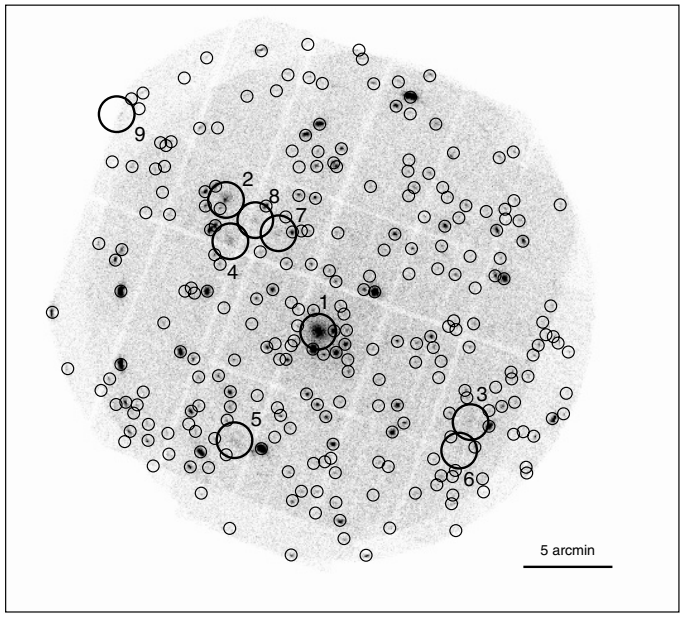

Fig. 1. Stacked EPIC image in the 0.2–2.0 keV band with detected point sources (small circles) and extended sources (large circles) labelled from 1 to 9.

The `emldetect` output source list contains 264 sources[2], of which nine are indicated to be extended. These objects are numbered in Fig. 1. Table 3 lists the extended sources with their basic X-ray parameters derived from `emldetect` and sorted according to source counts. Spectral X-ray properties normalised to physical scales are found in Table 4.

2.2. X-ray spectra and redshift estimates

Thanks to the deep exposure in the field, several of the extended sources were detected with more than 1000 source counts (see Table 3). We therefore attempted to estimate the redshifts of the brightest cluster candidates by fitting EPIC spectra with plasma spectra templates, keeping redshifts and temperatures as free parameters. With the same method we derived metallicities for those clusters where it was feasible.

[2] The complete source list of point source is found in Table 2 (available at the CDS). The extended source, however, are listed in Table 3.

We extracted spectra (using `XMM-SAS v.10.0`) for all the sources with >400 counts (i.e. sources ext#1-#6). Due to the low count rates (0.01–0.05 cts s^{-1}) and the extended nature of the sources the background fraction in the extracted spectra is relatively high. Therefore the regions for source and background extraction were manually selected to avoid systematic errors introduced by chip gaps, etc., and to avoid contamination by unrelated X-ray sources. The data were rendered and fitted through `XSPEC` using C statistics. We applied single MEKAL models corrected for galactic absorption (`tbabs`).

The spectral fits enable us to get a handle on the clusters redshift, which initially drove our follow-up programme. Some X-ray spectra enabled tight constraints on the distance, as in the case of source ext#1, which is the only source alone the iron line has been detected. Others merely confirmed the "high" redshift $z \gtrsim 1$ nature of the cluster as displayed in Figs. A.1a–e. An overview of spectral X-ray properties is presented in Table 4. The individual results are discussed both in Sect. 5 for each confirmed cluster individually and in Appendix A. The spectral properties in the context of the proper flux determination are discussed in the next section.

2.3. Flux determination

To enable comparisons of our results with previous findings from other works requires a flux measurement within a fixed radius. There, S_Δ is the flux within R_Δ, where Δ is defined as the average density of the intracluster medium (ICM) relative to the critical density of the Universe at a given redshift. The flux S_{500} is commonly indicated, however, in most cases not directly measurable, owing to the sensitivity of the instruments, the background level, point source contamination and chip gaps. The fluxes from Table 3 are the results of the source detection, and they correspond to fitted beta models integrated over a theoretically infinite radius.

To obtain S_{500}, we apply an iterative approach. This method is described in detail in Šuhada et al. (2012) and Takey et al. (2011). To estimate M_{500} we apply the empirical scaling relation from Vikhlinin et al. (2009). Since these authors measure the flux in the energy band 0.5–2 keV as well, no conversion is required. Appropriately, the evolution of the $L_X - M$ relation deduced in Vikhlinin et al. (2009) is compatible with the findings from Reichert et al. (2011), which both allow for a non-evolution scenario; i.e., the luminosity of clusters does not change self-similarly with redshift. In the self-similar case, the evolution factor is $E(z)^{-7/4}$. The physical parameters used in the iterative

Table 4. Extended X-ray sources.

#	$S_{0.5-2.0\,\mathrm{keV}}$ 10^{-15} erg cm^{-2} s^{-1}	$L_{0.5-2.0\,\mathrm{keV}}$ 10^{42} erg s^{-1}	T keV	Abund. $Z_\odot$	r_{spec} arcsec	R_{500} Mpc	L_{500} 10^{42} erg s^{-1}	M_{500} 10^{14} $M_\odot$
1	21.32 ± 0.03	11.7 ± 0.02	2.14 ± 0.07	$0.34^{+0.06}_{-0.09}$	48	0.56	14.5 ± 0.3	0.79
2	6.28 ± 0.03	54.0 ± 1.50	4.40 ± 0.48		23	0.39	70.7 ± 5.3	1.07
3	2.28 ± 0.01	0.86 ± 0.002	1.42 ± 0.18		29	0.40	1.69 ± 0.09	0.17
4	2.87 ± 0.28	13.4 ± 0.13	2.06 ± 0.20		23	0.41	21.6 ± 4.0	0.57
5	2.93 ± 0.32	25.1 ± 0.27	2.00 ± 0.21		26	0.39	33.5 ± 7.9	0.71
6	1.05 ± 0.01	0.59 ± 0.07	1.84 ± 0.86^a		30	0.34	0.92 ± 0.2	0.12

Notes. X-ray properties from spectral fitting and the iterative method (Sect. 2.3). Sources ext#7–#9 have been excluded, for they are not galaxy clusters. In case of non-symmetric errors, the largest deviation is presented. The first four columns display spectral measurements. r_{spec} is the radius in which the spectrum has been extracted. R_{500}, L_{500} and M_{500} are products of the iterative method. $^{(a)}$ Tentative value, due to low signal-to-noise.

approach are computed using the following equations:

$$M_{500} = 1.64 \times 10^{-13}\, L_{500}^{0.62}\, E(z)^{-1.15} \left(\frac{h}{0.72}\right)^{0.24} \quad (2)$$

$$R_{500} = \left(\frac{3\, M_{500}}{4\pi\, 500\, \rho(z)}\right)^{\frac{1}{3}} \quad (3)$$

$$r_{\mathrm{c}} = 0.07\, R_{500}\, T_{500}^{0.63}, \quad (4)$$

where $\rho(z)$ is the critical density of the Universe, and h the normalised Hubble parameter. The evolution factor and $\rho(z)$ are defined as

$$E(z) = \sqrt{\Omega_{\mathrm{m}}\,(1+z)^3 + \Omega_{\mathrm{a}}} \quad (5)$$

$$\rho(z) = \frac{3\, E(z)^2\, H(z)^2}{8\,\pi\, G}. \quad (6)$$

Given the luminosity from the spectral fit, we can make an estimation for M_{500} by applying Eq. (2) and setting h to 0.70. The errors on the mass are the simple propagation of the luminosity uncertainties. From this quantity we derive R_{500} using Eq. (3). Since the cluster-specific core radius, which largely determines the shape of the beta model, is only mildly realistically described by the `emldetect` output, we use the empirical relation, Eq. (4), from the cosmic evolution survey (COSMOS, Finoguenov et al. 2007) to re-estimate r_{c}. The essential step in this procedure is to determine what fraction of R_{500} we have covered in the area from which the spectrum has been extracted.

To do so, we synthesise beta models as in Eq. (7). The beta model is essentially a King profile from Eq. (1), and it describes the surface brightness profile of a cluster, determined uniquely by the core radius r_{c}, provided β is known. By varying the radius R, which is computed using Eq. (3), we determine the fraction of the surface brightness enclosed, which equals the luminosity correction for a certain radius.

When this quantity converges, i.e. $R = R_{500}$, after several iterations (typically 2) we assume we have obtained the true R_{500}, and hence L_{500} proper. On average the spectral extraction radius has been 2.2 times smaller than R_{500}. The resulting values are presented in Table 4 using spectral fluxes.

$$S(R) = S_0 \left(1 + \left(\frac{R}{r_{\mathrm{c}}}\right)^2\right)^{-3\beta+\frac{1}{2}}. \quad (7)$$

We fix the temperature at the value from the spectral fit. We emphasise, that all source detection chains in this work assume $\beta = \frac{2}{3} \approx 0.67$. The factor between $L_{0.5-2.0\,\mathrm{keV}}$ and L_{500} in Table 4 is applied to convert $S_{0.5-2.0\ \mathrm{keV}}$ into S_{500}.

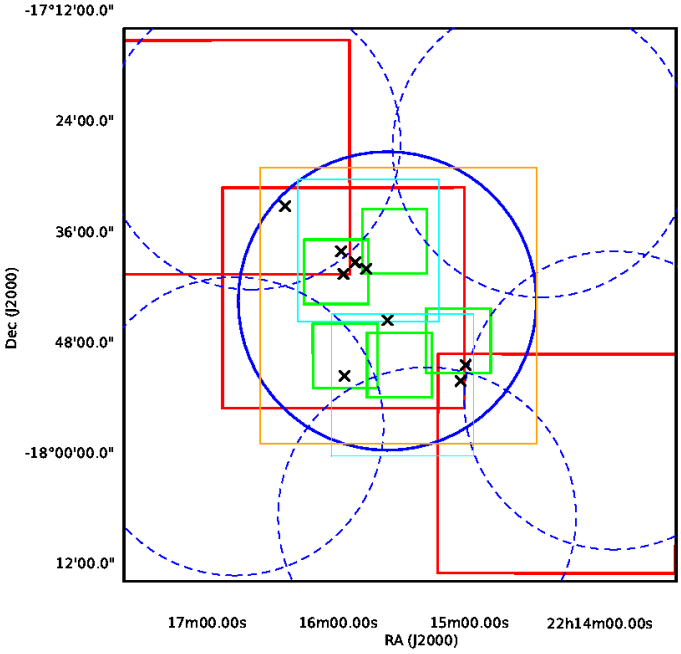

Fig. 2. Sky coverage of imaging campaigns.Black: the optical 1 deg^2 CFHTLS D4 field. Orange: the *BVRI* sky projection as imaged by the WFI. Red: the NIR WIRcam supplementary coverage. Cyan: the NIR observations made at Calar Alto. Blue: *XMM-Newton* pointings. The dashed circles represent the 2007 study (P.I. K. Nandra) covering the entire D4 in X-rays with ~30–40 ks exposures (Bielby et al. 2010). Green: VLT-FORS2 pointings used for initial detection. The crosses indicate the position of all clusters found.

3. Optical imaging

The field of LBQS 2212-1759 has been the target of various imaging programmes. This section describes campaigns that have been launched as part of this study and the archival data analysed in supplement. An overview of the sky coverage is presented in Fig. 2. In this paper, only the area enclosed by the central *XMM-Newton* pointing (blue circle, solid line) is considered.

First, the field was selected for deep imaging observations in the *B*, *V*, *R*, and *I* bands with the Wide Field Imager (WFI) at the 2.2 m ESO/MPIA telescope as part of the ESO Imaging Survey (Dietrich et al. 2006). The exposure time in the *R*-band was augmented by a guest observer programme for the Bonn weak lensing survey (Dietrich et al. 2007, BLOX). In Oct. and Nov. 2006, a NIR campaign was run in the bands z and H with the Omega 2000 camera at the Calar Alto 3.5 m telescope. Both ESO data sets have been used for the initial clusters identification. For all

final photometric analysis in this section, however, we rely solely on the data from the CFHTLS, due to its supremacy. We describe the data reduction in Sect. 3.1. Section 3.2 describes the retrieval of photometric redshifts, which we apply to find over-densities of galaxies in Sect. 3.3.

3.1. CFHT data

We make use of *ugriz* archival data taken with the MegaPrime/MegaCam instrument mounted at the prime focus at the 3.6 m CFHT. This instrument has a field of view (FoV) of 1×1 deg^2 and a scale of 0.187 arcsec per pixel.

We made use of data located in the deep field D4 of the CFHT Legacy Survey (CFHTLS), which is part of the CFHT Supernova Legacy Survey (SNLS) and observations are still ongoing. We retrieved the data from the Elixir system[3] in a pre-processed form and further processed it as described in Erben et al. (2009)[4]. This reduction is independent of the official releases by the CFHTLS collaboration (Ilbert et al. 2006; Coupon et al. 2009).

The photometry was performed with `sextractor` (Bertin & Arnouts 1996) in dual mode using the *i*-band image as a detection frame. We measured magnitudes in apertures of 1.86 arcsec of diameter in seeing-matched images. The derived magnitudes were used to derive colours, SED classification, and photometric redshifts (see below). We also made use of deep near-infrared data (*JH* & *Ks* bands) with the WIRcam (also at CFHT). The data is part of the WIRcam Deep Survey (see Bielby et al. 2010) and covers a significant portion of most of the deep *XMM-Newton* field. This data is important for obtaining precise photometric redshifts at high redshift as important continuum features (e.g. the 4 000 Å break) are shifted to the near-infrared.

3.2. Photometric redshifts

In this paper we use the multi-band imaging ($u^*g'r'i'z'JHKs$) and photometric galaxy redshifts from the CFHTLS to identify cluster counterparts of the extended X-ray sources and to measure their photometric redshifts. We used the code `PHOTO-z` (Bender et al. 2001) to estimate the photometric redshifts, with a set of 31 SED templates (see Brimioulle et al. 2008; Lerchster et al. 2011, for details).

We used the results from the spectroscopic programme (Sect. 4) to calibrate our photometric redshift estimates by applying zero-point offsets (typical values are ~0.01 . . . 0.1 mag). A total of 106 spectra fulfil the quality criteria (i.e. objects with reliable photometric *and* spectroscopic redshifts). The fraction of catastrophic outliers is defined as $\eta = |z_{\rm spec} - z_{\rm phot}|/(1 + z_{\rm spec}) > 0.15$, which is 2.8% in our case. The redshift accuracy is measured with the normalised median absolute deviation, $\sigma = 1.48 \times {\rm median}(|\triangle z|/(1+z)) = 0.037$, where $\triangle z = z_{\rm spec} - z_{\rm phot}$ and z is spectroscopic. The value of σ is identical to the standard deviation of $|\triangle z|/(1 + z)$.

3.3. Galaxy over-densities

From the photometric redshift information we measured the projected galaxy over-density in overlapping redshift intervals of $\Delta z = 0.05$. The purpose of this procedure was to qualitatively illustrate the completeness of the X-ray selection technique as a method to identify clusters of galaxies. Therefore we set a relatively high detection threshold in order to pick up only the most significant density peaks.

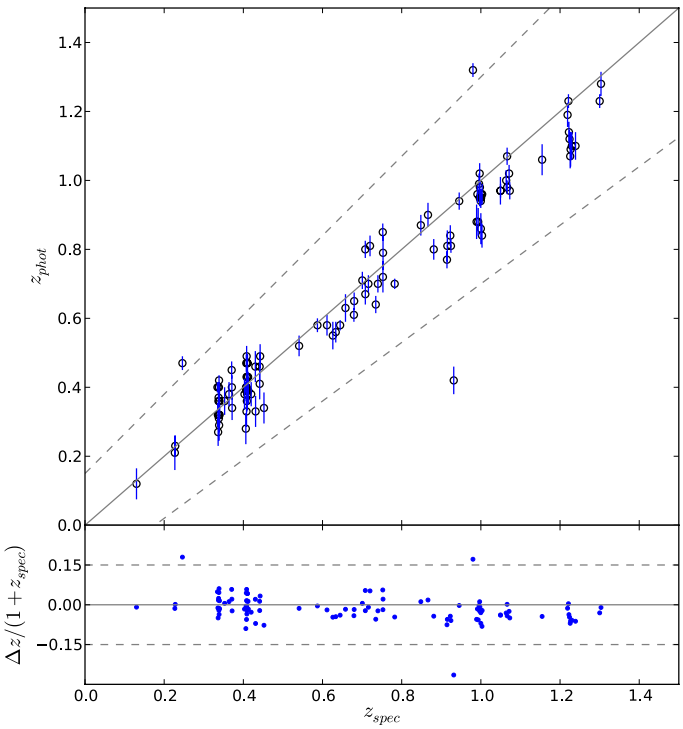

Fig. 3. Photometric redshifts, plotted against the spectroscopic ones. The vertical dashes are the photometric redshift errors. The dashed lines are for $z_{\rm phot} = z_{\rm spec} \pm 0.15\ (1 + z_{\rm spec})$.

We computed the mean galaxy density in boxes of 400 kpc a side, which is enlarged to 500 kpc for redshifts $z > 0.9$, masking out regions affected by bright stars. At redshifts beyond $z > 0.9$ clusters are thought to be increasingly less relaxed. Therefore, the need arises to search for the associated galaxies in a larger physical volume. The values of Δz, the box size and the critical redshift where the box size changes have been tuned to maximise the detection of the already known clusters in this field from this work. We consider only galaxies with a photometric redshift error $\delta z < 0.1$. We compared the number of galaxies in the box to the assumed Poisson distributed background, which is taken to be the mean galaxy count in the field considered. The likelihood (Eq. (8)) was computed taking the negative natural logarithm of the incomplete gamma function $P(a, x)$ as defined in Eq. (9). The incomplete gamma function is an integral, which is applied to computing the likelihood that a given distribution x (i.e. the number of galaxies is the box) is exceeding Poissonian noise a (Cash 1979).

$$L = -\ln P(a, x) \tag{8}$$

with

$$P(a, x) = \frac{1}{\Gamma(a)} \int_0^x {\rm e}^{-t} t^{a-1} {\rm d}t, \tag{9}$$

where $\Gamma(a)$ is the gamma function. This method of "source finding" is similar to the `XMM-SAS` task `eboxdetect` (Watson et al. 2009) also described in Sect. 2.1. The resulting map is displayed in Fig. 4 as contours on the stacked X-ray image. The redshift intervals are chosen to overlap in order to prevent a search bias

[3] http://www.cfht.hawaii.edu/Instruments/Elixir/home.html

[4] The full procedure of data reduction and calibration will be described in Brimioulle et al. (in prep.), see also Brimioulle et al. (2008).

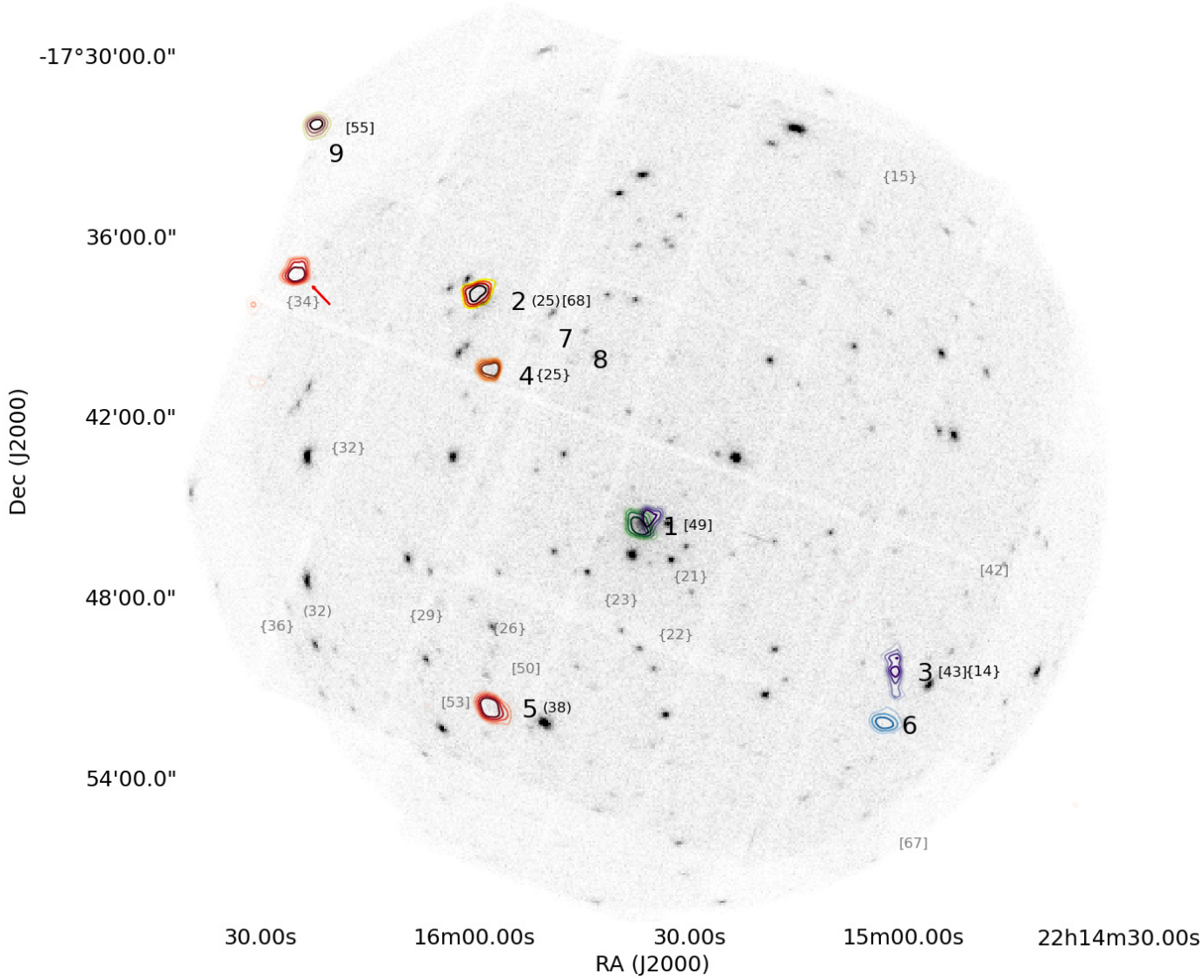

Fig. 4. Over-density contours of galaxies within the field of view of the *XMM-Newton* pointing. The background image is the stacked image of all *XMM-Newton* observations of LBQS2212 (0.5–2.0 keV). The extended X-ray sources from Fig. 1 are indicated with their identifiers on the side (1 arcmin offset in RA). In smaller fonts the identifiers from other works are indicated either in black, if presented in this work as well, or in grey if not found by our method. Between round brackets the identifier from Bielby et al. (2010) is indicated and square brackets refer to the catalogue from Olsen et al. (2007). Curly brackets present the clusters from Adami et al. (2010). The red arrow points at an optical over-density, which has no clear counterpart in X-rays. The contours represent 5 Poissonian likelihood levels with $10 < L < L_{\rm max}$, colour-coded, or rather colour-mapped, by redshift interval: purple $z = 0.3$ $L_{\rm max} = 15$, blue $z = 0.35$ $L_{\rm max} = 20$, green $z = 0.45$ $L_{\rm max} = 20$, dark pink $z = 0.78$ $L_{\rm max} = 30$, orange $z = 0.98$ $L_{\rm max} = 15$, red $z = 1.18$ $L_{\rm max} = 20$, heat $z = 1.38$ $L_{\rm max} = 20$, where z refers to $z_{\rm min} + \frac{1}{2}\Delta z$, i.e. the middle of the bin.

that would occur when clusters fall exactly between two intervals. Since the redshift error cut is set to 0.1, some galaxy over-densities are expected to show up in multiple adjacent redshift bins. We have assumed a nominal redshift error of 0.001 for all galaxies, ensuring that each galaxy appears in one redshift bin only. All confirmed X-ray selected clusters from Table 7 are retrieved at the appropriate redshifts. That is, all spectroscopically confirmed clusters are found in a redshift interval around the nominal redshift taking the spread in the photo-z accuracy into account (see Fig. 3), of which typical values amount to about 5%.

We define the photometric redshift $z_{\rm phot}$ of the clusters as the *mean* of all galaxies meeting the above-mentioned selection criteria (i.e. photometric accuracy and spatial distribution), having $\frac{\Delta z_1}{1+z_{\rm mid}} < 0.05$, where $\Delta z_1 = \mid z^* - z_{\rm mid} \mid$. $z_{\rm mid}$ is the middle of the redshift bin containing the largest number of galaxies, whereas z^* is the photometric redshift of each individual galaxy. redshift. The relative difference (in %) in Table 7 is defined as $\frac{\Delta z_2}{1+z_{\rm spec}}$, where $\Delta z_2 = z_{\rm phot} - z_{\rm spec}$. For the nearby clusters in our sample, $z_{\rm phot}$ tends to be slightly overestimated, while the high redshift ones the photometric redshift is somewhat lower than the spectroscopic one. The redshift bin, in which the galaxy signal is strongest (i.e. highest likelihood) is selected for display in Fig. 4. This quantity is identical neither to $z_{\rm mid}$ nor to $z_{\rm phot}$ due to different treatments of background galaxies. Nonetheless, they remain similar.

The clusters are indicated with colour-coded contours reflecting the redshift and the over-density likelihood. We display

only significant[5] over-densities having $L > 10$, within the FoV of the *XMM-Newton* pointing. A selection of clusters found in previous publications (Bielby et al. 2010; Olsen et al. 2007; Adami et al. 2010) are also referred to in Fig. 4. The most distant (Stanford et al. 2006) cluster is detected by all groups except for Adami et al. (2010), whereas some other structures, i.e. system ext#6 and the new, possibly spurious structure (red arrow in Fig. 4), are found solely in this work. Source ext#4 is also found by Adami et al. (2010) at $z_{\rm phot} = 0.95$. Finally, we retrieve all X-ray selected clusters as optical over-densities. Additionally, we find a significant over-density, that is idicated by the arrow in Fig. 4, which could not be associated with an X-ray source at an off-axis angle ∼14 arcmin. The optical data suggest a detection due to an projection effect, since no conglomeration of *red* galaxies is evident.

Olsen et al. (2007) have applied the Postman matched filter (MF, Postman et al. 1996) to search for optically selected clusters of galaxies in the CFHTLS deep fields. In the overlap of field D4 with the *XMM-Newton* FoV they found eight clusters with redshifts ranging from $z = 0.3$ to $z = 1.1$. These structures are partially retrieved by us as seen in Fig. 4. Grove et al. (2009) have extended the sample by including the z'-band. This has led to an enhanced detection of distant clusters, which, however, are not discussed further in this work.

In a similar fashion Adami et al. (2010) detect ten clusters within the common area from galaxy density maps resulting from an adaptive kernel algorithm working on slices in (photometric) redshift space. The papers from Olsen et al. (2007), Grove et al. (2009), and Adami et al. (2010) are comparable to one another in various ways, and for the same reasons different from our study. First of all, all base their density map on a single band detection (for instance the i' band), secondly, use a similar detection algorithm for optical over-densities, and thirdly, none perform an X-ray source detection, which automatically points them to a larger quantity of less massive optical clusters. Last, the works addressed above are restricted to the optical $u^*g'r'i'z'$ data and therefore are expected to remain less sensitive to the more distant clusters in the field.

Gavazzi & Soucail (2007) use the i'-band images for weak lensing mass reconstruction. In the D4 field they find one significant mass peak, which is outside the *XMM-Newton* FoV.

A more direct camparison to our work is given by Bielby et al. (2010), who applied a red sequence finder to their wavelet-detected extended X-ray sources in D4. This team focussed on groups and clusters at high redshift $z \gtrsim 1.1$, disgarding all sources at lower redshift. The number density of sources (40 per deg^2) they find is roughly equal to the results from our search algorithm using XMM-SAS. These authors report on three distant X-ray luminous groups within the area covered in this paper, of which two (see Fig. 4) have been retrieved by us as well both as X-ray and optical over-density structures. Interestingly, Bielby et al. (2010) make no reference to the source ext#4, described in Sect. 5.4. One of their sources, ID-32 or WIRDXC J2216.4-1748, could not be confirmed by us. Likewise, we have been able to spectroscopically refine the two photometric cluster redshifts found by these authors.

4. Optical spectroscopy

The spectroscopic results used in this publication were obtained with FORS2 mounted on the VLT through observing programme 079.A-0369(C) (Aug./Sept. 2007) and 080.A-0659(A) (Oct./Nov. 2007 and Jun. 2008). The total integration time of roughly 19 hours was used to target the nearby cluster candidates ext#1, ext#3 and ext#6 with three masks through grism `150I` and the distant cluster candidates ext#4 and ext#5 with four masks through grism `300I` grism. As spectroscopic targets we prioritised those objects that lie close to the X-ray emission peak and/or have colours close to the red sequence as determined from the ESO-VLT imaging. We also targetted some X-ray point sources.

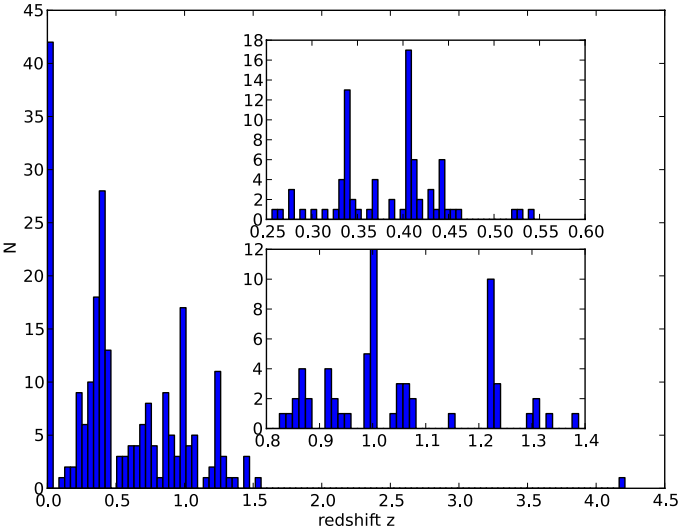

Fig. 5. Histogram of all 231 science grade spectra. The insets show a zoom-in on the low (*top*) and high (*bottom*) redshift range.

The science data was flat-fielded and wavelength-calibrated with the appropriate calibration files supplied by the FORS2 database. The bias was read from the chip overscan region. Flux calibration has been applied with a single response curve derived from only one observation. No atmospheric correction has been performed. The recorded spectra have a spectral coverage from 6000−10 000 Å ($\Re = 660$) and 4000−10 000 Å ($\Re = 260$) for the `300I` and `150I` respectively, where $\Re$ denotes the resolving power.

From 289 slits we were able to extract 231 science-grade spectra, plus 19 double recordings, having sufficient signal-to-noise to classify the spectra and measure redshifts, of which six are QSOs and 42 (late-type) stars. Their redshift distribution is shown in Fig. 5. A total of 66 spectra are of cluster members, excluding ten double recordings. The remaining 118 spectra belong to unrelated field galaxies. The complete catalogue can be viewed as in Table 5 (available at the CDS). The list of cluster members is presented in Table 6. Galaxy cluster members have been selected within an redshift interval $\Delta z \lesssim 0.015$ around the mean redshift within a projected radius of $\lesssim$1 Mpc around the X-ray source.

Redshifts were obtained by correlating the spectra with the elliptical and oldest starburst template from Kinney et al. (1996), both with the EZ software (Garilli et al. 2010) for passive galaxies and the `IRAF FXCOR` task for some galaxies with strong emission lines.

Galaxy spectra were processed from 4500 Å up to 10 000 Å, depending on spectral coverage and faulty regions. Regions with strong sky absorption have been masked out. In most case this range samples the following most prominent features: [OII] $\lambda\lambda$3726, 3729 emission lines, the

[5] $L = 10$ corresponds to a significance >99.9% or roughly 5σ in Gaussian statistics.

Table 6. Overview of spectroscopic redshifts for all confirmed cluster members with distances from the X-ray centre $\lesssim$ 1 Mpc/$\lesssim$ 1.7 Mpc/>2.5 Mpc (white/grey/dark grey background).

ID	Redshift z				
	ext#1	ext#3	ext#4	ext#5	ext#6
A	0.407	0.337	0.999	1.237	0.408
B	0.411	0.337	0.996	1.220	0.405
C	0.409	0.335	1.001	1.222	0.408
D	0.408	0.339	1.005	1.226	0.408
E	0.406	0.337	0.992	1.223	0.413
F	0.406	0.335	0.995	1.224	0.406
G	0.410	0.338	1.003	1.229	0.409
H	0.406	0.343	1.000	1.222	0.419
I	0.408	0.337	1.001	1.228	0.410
J	0.409	0.341	0.999	1.225	0.403
K	0.402	0.339	0.998	1.223	0.409
L		0.339	0.999	1.240	0.407
M		0.338	1.001		0.410
N		0.344			0.418
O		0.337			
P		0.336			
Mean	0.408	0.338	0.999	1.227	0.410

Notes. The ID corresponds to the identifiers in Figs. 6b, 11, 14, 17, 20 in as far they appear within the cut-out. The entries are ordered according to their distance to the X-ray emission peak. The last row contains the mean for each column. Formal redshift errors (1σ) are typically <0.001 and not listed here. A complete listing of all science-grade spectra can be found in Table 5.

CA H+K $\lambda\lambda$3934, 3969 absorption lines, the 4000 Å-break, the G-band around $\lambda \sim 4300$, the hydrogen lines Hδ λ4102 and Hβ λ4861, and [OIII] $\lambda\lambda$4959, 5007. Strong emission line galaxies were sampled in a region around the most prominent emission lines. Only the two mentioned templates were used to avoid systematic redshift shifts due to resolution between templates.

No redshift errors are indicated in Table 6, since the variance in redshift resulting from using different templates (i.e. other templates than the two mentioned above) is generally large (~0.001) because of the spectral resolution of the instrument, which is limited to $\delta z \sim 0.01$. The formal 1σ confidence intervals resulting from the χ^2 template fit, however, are much smaller, typically <0.001. For emission line galaxies the errors are smallest and are given by our spectral wavelength calibration (~0.1 Å), which results in $\delta z \sim 0.00001$. Line feature centroids can be determined with much higher precision than the instrumental resolving power. In Table 5, however, we merely present the formal 1σ errors.

5. Identifications of *XMM-Newton* cluster candidates

In the deep CFHT imaging six out of the nine extended X-ray sources can be identified with clusters of galaxies. All mentioned redshifts are mean averaged spectroscopically determined redshifts, unless stated otherwise. Table 7 gives the likely identifications with their photometric redshifts if available. Column "redshift X-ray" gives the 1σ range of the X-ray spectroscopic redshift estimates derived from $kT - z$ contours (see Figs. A.1a–e). The cross-reference redshifts listed in column "redshifts publ." refer to the optically selected catalogues from previous publication. In Figs. 6a–24 the colour–magnitude diagrams $H_{\rm mag}$ vs. $(z' - H)_{\rm mag}$ for all X-ray positions are displayed, which are discussed qualitatively for each position individually. The terms *red sequence* and the *expected colour* of a cluster are used invariably, since we assume, as a zeroth-order approximation, a zero gradient of $z' - H$ (mag) as a function of relative brightness. The values of the empirically determined cluster colour as a function of redshift are taken from Fassbender et al. (2011a). We chose to remain with a single colour, i.e. $z' - H$, in order to illustrate its effectiveness thereof for the redshift's range $0.3 < z < 1.5$ and to be able to relate our results to Fassbender et al. (2011a; their Fig. 3). Yet, a single colour does not always optimally sample the 4000 Å break, however, the chosen filter combination is a monotonic function of the red sequence of passively evolving galaxies, hence sufficient for our purpose.

5.1. XMMU J221536.8-174534 (ext #1) z = 0.41

Nearly on axis we find the brightest extended source at a redshift of $z = 0.408$. The position of brightest galaxy coincides with the X-ray emission peak, as can be expected for relaxed clusters at relatively low redshifts. The extended X-ray source has been described as alikely cluster of galaxies by Clavel et al. (2006). This is confirmed by our optical imaging. The X-ray spectrum (see Fig. A.1a) is consistent with the photometric redshift $z = 0.4$ as found in the MF searches by Olsen et al. (2007) and Dietrich et al. (2007). The CFHT z'-band image with X-ray contours and spectroscopic members is shown in Fig. 6b. The cluster has a well-evolved red sequence as seen in Fig. 6a consistent with the empirically expected $z' - H$ colour. Six of its 11 spectra are presented in Fig. 6c.

In Fig. 4 system ext#1 is associated with two over-density contours: the purple ones at $z \sim 0.3$ and the greens ones at $z \sim 0.45$. It is possible, therefore, that the X-ray emission is a superposition of two clusters at different redshifts. From the X-ray redshift-temperature contours and from the positioning of galaxies with respect to the X-ray emission peak, however, we are able to conclude that the X-ray emission originates in the more distant redshift of the two. The structure at $z \sim 0.3$ was detected only as galaxy over-density and is not regarded as contributing to the X-ray emission. Additionally, we retrieved two spectroscopic redshifts at $z \sim 0.34$ at about 50 arcsec from the peak of source ext#1, which are listed as object O and P in the ext#3 column in Table 6.

5.2. XMMU J221558.6-173810 (ext #2) z = 1.45

The most distant galaxy cluster in this field has already been reported by Stanford et al. (2006). It has been the topic of several dedicated studies since then, e.g. studying star formation at high redshift (Hilton et al. 2010; Hayashi et al. 2011). This is one of the most distant known X-ray selected cluster of galaxies with unambiguously strong X-ray emission, albeit with a confirmed contamination from point sources (Hilton et al. 2009). In addition to earlier publications, we find several galaxies with photometric redshifts compatible with $z \sim 1.45$. The over-density contours in Fig. 4 for this cluster are displayed with the *heat* colour scheme. An CFHT z'-band image is shown in Fig. 8 with X-ray contour overlays and the positions of three new quasars indicated, of which two reside at the cluster redshift. The colour–magnitude diagram in Fig. 7 shows that a red sequence is already present at this high redshift, following the empirically expected colour. We have not obtained additional galaxy spectra in our observation runs.

However, we serendipitously identified two quasars at the nominal cluster redshift on the very outskirts of the cluster (see

Table 7. Optical identifications of extended sources.

Seq. #	Source XMMU J..	Identification	Redshift z_{spec}	z_{phot}	z_{BCG}	publ.	X-ray	$\Delta z/(1+z)$ %
1	221536.8–174534	cluster	0.41	0.46	0.47 ± 0.05	0.4[a] ,0.3[d]	0.37–0.4	+3.7
2	221558.6–173810	cluster	–	1.34	1.37 ± 0.06	1.45[b] ,1.37[e] , 1.2[a]	0.9–1.6	−4.5
3	221500.9–175038	cluster	0.34	0.29	0.42 ± 0.03	0.3[a] ,0.38[e]	–	−3.4
4	221557.5–174029	cluster	1.00	0.90	0.98 ± 0.04	0.95[e]	0.9–1.2	−5.0
5	221556.6–175139	cluster	1.23	1.12	1.23 ± 0.04	1.17[c]	> 0.9	−4.8
6	221503.6–175215	cluster	0.41	0.42	0.49 ± 0.06	–	–	+0.8
7	221546.2–174002	empty field	–		–	–	–	–
8	221551.7–173918	empty field	–		–	–	–	–
9	221624.3–173321	point source	–		–	–	–	–

References. The column "redshift publ." lists redshifts from already published works. The last column gives the difference, in percent, between the spectroscopic redshift and the photometric redshift of the BCG. [(a)] Olsen et al. (2007); spectroscopic redshift, [(b)] Stanford et al. (2006); [(c)] Bielby et al. (2010); [(d)] Grove et al. (2009) ; [(e)] Adami et al. (2010).

Fig. 8). The spectra are presented in Fig. 9 (identifiers A and B). For future spectroscopic X-ray analysis, these X-ray sources do not need to be included as power laws contributing to the X-ray flux since they lay beyond 1 arcmin, i.e. farther than the spectral extracting radius. In a joint *Chandra-XMM-Newton* analysis, Hilton et al. (2010) report a temperature of 4.1 kT with the inclusion of three power laws to account for point source contributions. In contrast, our analysis, as stated before, assumes the emission to result from only a single hot plasma. The extraction region used by Hilton et al. (2010) is only mildly (7 arcsec) larger than the one we used.

5.3. XMMU J221500.9-175038 (ext #3) z = 0.34

At a mean redshift $z = 0.338$ cluster ext#3 is the closest galaxy cluster in the field. This cluster was also detected in the MF searches by Olsen et al. (2007) ($z \sim 0.3$) and Dietrich et al. (2007). We show the CFHT z'-band image with X-ray emission contours and labelled spectroscopic members in Fig. 11. The red sequence is easily visible in Fig. 10 at the colour expected for its redshift. Its selected 14 spectroscopic members are within $|z - z_{cluster}| \lesssim 0.006$. Figure 12 shows six of the confirmed members.

In the same redshift bin as cluster ext#3 (green contours in Fig. 4) we find an over-density of galaxies virtually at the same projected position on the sky as the central cluster ext#1. One interpretation is to consider these over-densities to be a sign of knots in the cosmic web ∼3 Mpc apart; that is, the two galaxy over-densities are part of the same large-scale structure. There is no X-ray detection from a group of galaxies at $z = 0.338$ at the coordinates of cluster ext#1. Namely, the X-ray flux is compatible with only coming from source ext#1 as discussed in Sect. 5.1.

5.4. XMMU J221557.5-174029 (ext #4) z = 1.00

On the very edge of the redshift unity barrier we find a new cluster with 13 members. This cluster has already been referred to by Adami et al. (2010) as a photometric cluster candidate; however, it appears in no other catalogue. Two members are at the very centre of the X-ray emission, and both can be considered BCG, since their fluxes are similar.

The red sequence is visible in Fig. 13 without deviations from the expected $z' - H$ colour. Striking, however is the absence of a clear magnitude gap between the BCGs and the other galaxies, which could indicate a recently formed system. The spectra, a selection of six from 13, are presented in Fig. 15. The two BCGs have spectroscopic redshifts $\Delta z = 0.003$, which is well beyond their formal (1σ) errors. The cluster redshift of $z \sim 1.0$ is consistent with the estimate from the X-ray spectrum. An image of the cluster is shown in Fig. 14 with X-ray contours and confirmed members. The apparent point-like morphology of the X-ray emission is purely due to chip gaps masking out the cluster edges.

5.5. XMMU 221556.6-175139 (ext #5) z = 1.23

The optical imaging shows a conglomeration of both nearby and distant galaxies. The CFHT z'-band image is shown in Fig. 17 with X-ray contour and spectroscopically confirmed cluster members. This cluster has already been hinted at by Bielby et al. (2010), however, at a photometric redshift of $z = 1.17$. The colour–magnitude of the cluster is somewhat peculiar as seen in Fig. 16. The galaxy closest to the X-ray emission peak is blue and star-forming. Its membership is confirmed both spectroscopically and photometrically. Although the colour of the red members is as expected, we note there seems to be a significant ongoing build up of the red sequence. These properties are similar to the cluster found at $z = 1.56$ by Fassbender et al. (2011b). This second farthest cluster in the field has 12 concordant redshifts with $|z - z_{cluster}| \lesssim 0.013$. Figure 18 shows a selection of six members. Mask offsets[6] during observation caused the signal-to-noise to remain very low. However, due to the existence of single emission lines in the very centre of the clusters, the redshift could be established as $z = 1.227$. A redshift based only on one emission line remains tentative; however, the morphology of the galaxy in combination with its extent on the sky does not render it a likely possibility that we are seeing a background high-z Lyα emitter.

For this source the X-ray spectrum indicates a redshift lower limit of $z > 0.9$. Both the X-ray and galaxy over-density contours show an NW-SE elongation.

5.6. XMMU 221503.6-175215 (ext#6) z = 0.41

The cluster with the weakest X-ray emission at a redshift of $z = 0.410$ can easily be understood as a sign of large-scale structure. Cluster ext#6 possibly is a knot in the filaments around the

[6] Due to accidental pointing errors.

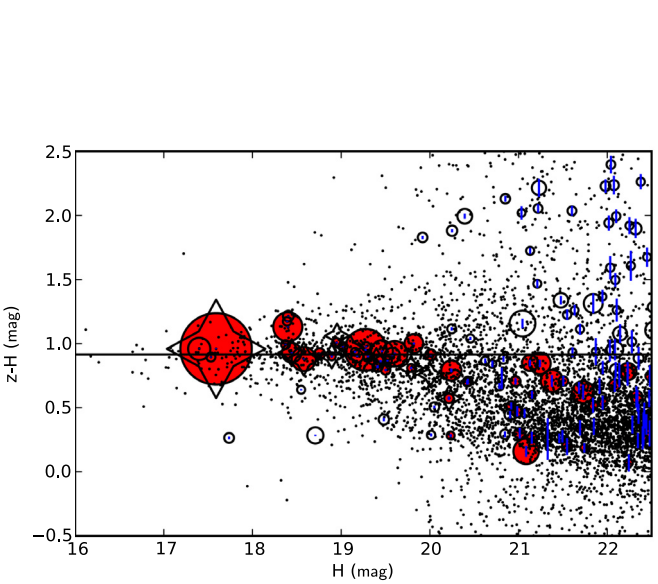

(a)

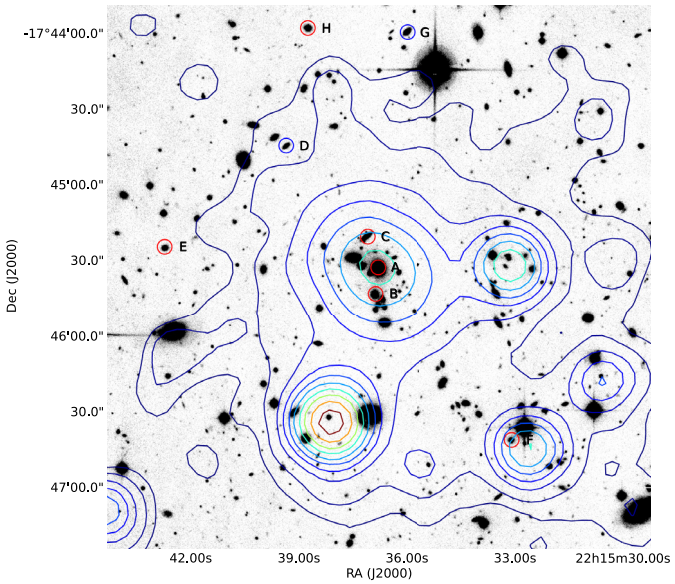

(b)

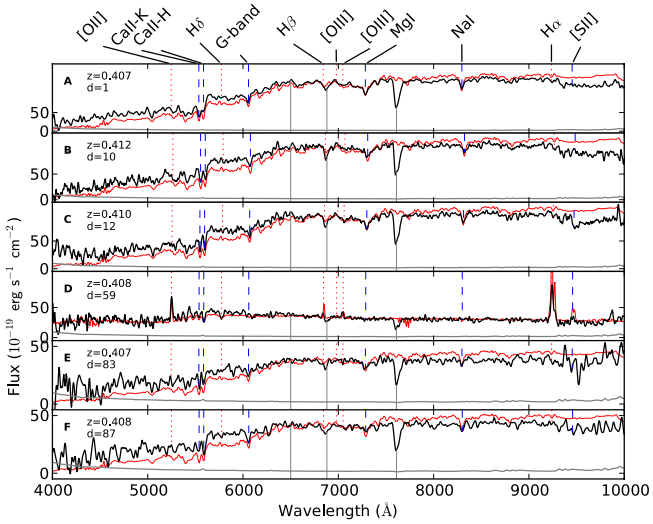

(c)

Fig. 6. a) Colour–magnitude diagram for the extended X-ray source ext#1. CFTHLS D4 z' and H-band images have been used. The small dots show *all* galaxies within D4 having cluster-concordant photometric redshifts, i.e. within the area between the dashed lines in Fig. 3. Open circles show all galaxies with good photometry <1 Mpc from the X-ray peak, of which the filled symbols have cluster-concordant photometric redshifts. Vertical dashes indicate the error in the colour. Star symbols indicate spectroscopic members. All symbols (apart from the dots) have been scaled, inversely, to their physical distance from the X-ray emission peak. In each panel, the horizontal line indicates the expected colour of luminous, red sequence galaxies at the given spectroscopic redshift, as obtained from the simple stellar population models calibrated on data available in Fassbender et al. (2011a). **b)** CFTHLS D4 z'-band image centred on the extended X-ray sources in the field. The blue and red circles indicate the positions of the spectroscopically confirmed star forming and passive cluster members, respectively. The contours overlay represent linearly spaced photon count levels of the X-ray sources. North is up, east is to the right. The image is 1.2 arcmin across. **c)** Selected spectra for cluster ext#1 in the observers' frame in black and their noise spectra in grey. Either an elliptical or emission template is overplotted in red. The positions of expected absorption and emission features have been indicated with blue dashed and red dotted lines, respectively. Vertical grey lines indicate regions affected by sky absorption. The spectra have been smoothed for clarity. The capital letters correspond to the entries in Table 6 and to the positions in Fig. 6b. The redshift z and the distance d (arcsec) to the formal peak of the X-ray source are indicated in the plot.

more luminous, hence more massive structure ext #1. This work provides the first reference to this cluster. The colour–magnitude diagram in Fig. 19 shows a well-evolved red sequence, which both confirms the maturity of the system and rejects the possibility of a chance-alignment. Since the colour is virtually identical to that of cluster ext#1, we have established further proof for the common redshift of the two clusters. We find 14 spectroscopic members (see Fig. 20) for the clusters of which six are plotted in Fig. 21.

The claim to perceive cluster ext#6 (Fig. 4) as part of the larger structure around system ext#1 is supported by the fact that we see emission line galaxies close to the centre of the cluster.

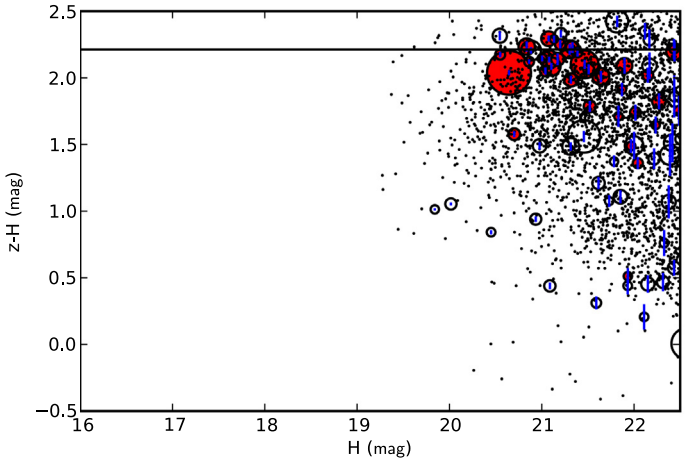

Fig. 7. As in Fig. 6a for source ext#2 at $z = 1.45$.

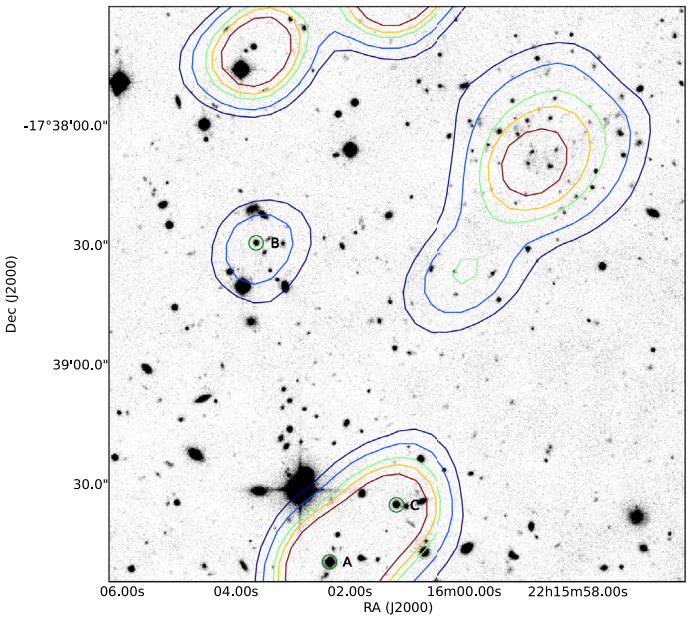

Fig. 8. As in Fig. 6b for source ext#2. The cluster is NE of the image centre. No new spectra have been obtained for this publication, apart from the three labelled X-ray point sources, whose optical spectra are shown in Fig. 9.

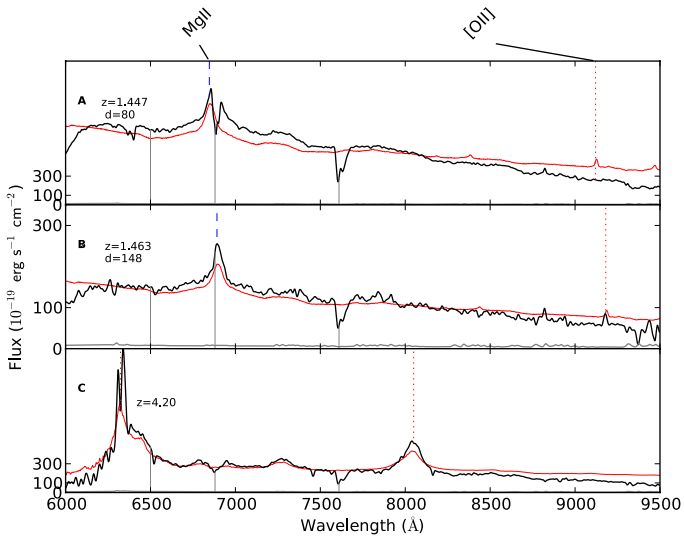

Fig. 9. Spectra (black) of the quasars discovered in the vicinity of cluster ext#2. In red a quasar template is overplotted. Objects A and B can be regarded as cluster members or rather active galaxies in the cluster outskirts. Object C is an unrelated distant X-ray luminous quasar serendipitously found in this study (Lamer et al. 2011). The labels correspond to the objects identified in Fig. 8. Spectral features, etc., are coded as in Fig. 6c. In the case of A the emission lines are Lyα and CIV.

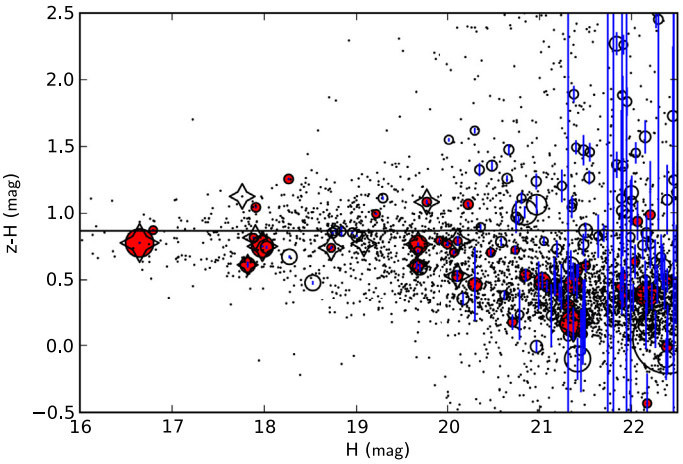

Fig. 10. As in Fig. 6a for source ext#3 at $z = 0.34$.

Three of the five galaxies nearest to the BCG (<1′) show at least Hα in emission. Evolved clusters are not expected to show strong signs of star formation, yet in the outskirts of the largest dark matter potentials, such as cluster ext#6, we do expect galaxies to be more active.

5.7. XMMU 221546.2-174002 (ext#7) and XMMU 221551.7-173918 (ext#8)

No clear cluster identification for these X-ray sources can be found in the optical data. Their vicinity on the sky makes it is natural to discuss these structures in symbiosis. Remarkably, neither in the very deep CFHT imaging nor in the WIRCam NIR data do we find a plausible visible counterpart for these sources as seen in Fig. 23, which rules out the possibility of a very distant cluster of galaxies within any reasonable redshift limit (i.e. $z \lesssim 2$). The colour–magnitude diagrams as displayed in Figs. 22a and b do not show any hint of a red sequence.

Source ext#7 has the lowest value for EXT_LIKE (extent likelihood in Table 3) in this sample and could be a blend of faint point sources and/or associated with source ext#8. The NVSS radio catalogue (Condon et al. 1998) contains a faint radio source (3.3 mJy at 1.4 GHz) at 18 arcsecond distance of source ext#8. The projection of the two object on the sky (NW versus SE with respect to the centre of Fig. 23) raises the idea of an associated bipolar phenomenon.

Furthermore, that both sources were not detected in the cluster's typical energy band (0.35–2.4 keV, see Sect. 2.1) suggests they may possess a relatively hard spectrum, which in turn favours another mechanism at work rather than bremsstrahlung.

Based on the extended nature of the sources, the radio detection, the hardness of the spectrum, as well as the absence of a clear optical counterpart(s), little alternative is left but to identify source ext#8 (and source ext#7) as a Compton ghost (Fabian et al. 2009).

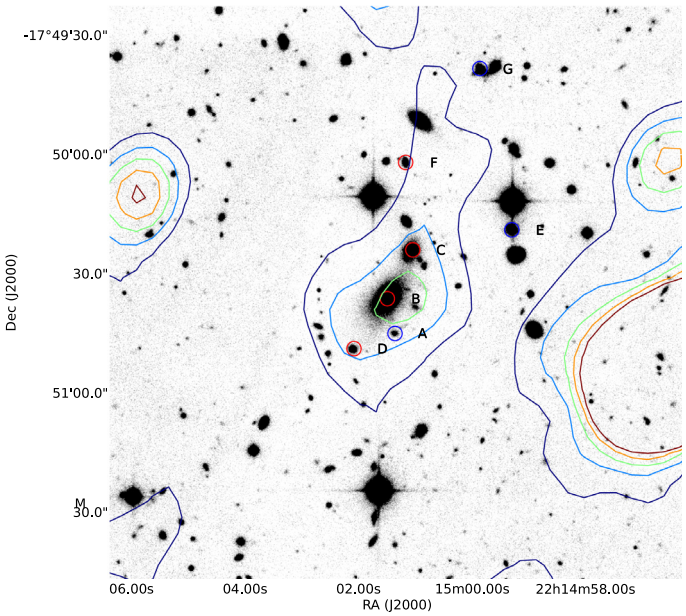

Fig. 11. As in Fig. 6b for source ext#3. The associated optical spectra are found in Fig. 12.

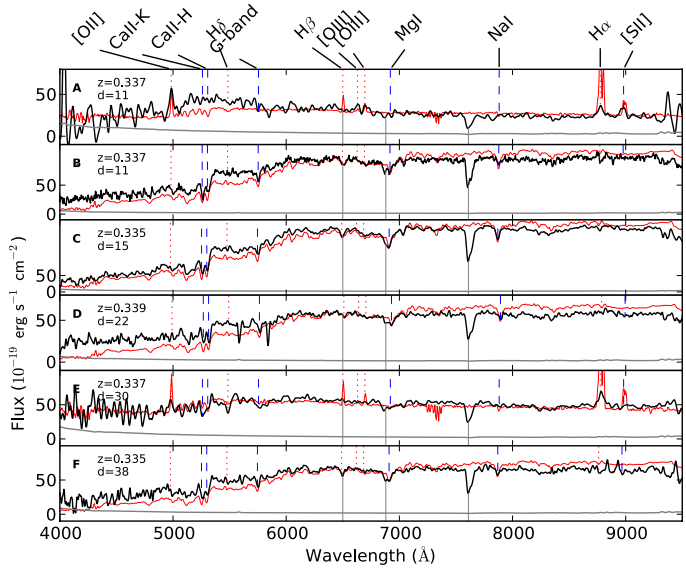

Fig. 12. Selected spectra for cluster ext#3 in the observers' frame. See Fig. 6c for explanation. The positions are seen in Fig. 11.

5.8. XMMU 221624.3-173321 (ext#9)

This source is excluded from further (cosmological) analysis, both for its being at a large off-axis angle, namely 16 arcmin (i.e. covered by the EPIC PN camera only), and its likely being a point source. Nonetheless, at about 1 arcmin from source ext#9 there is a complex X-ray structure (at an off-axis angle of 16 arcmin as well), which was not flagged as extended by our source detection. The two sources are displayed in Fig. 25, centred on the second source, while source ext#9 is SW towards the bottom. The structure at RA 22:16:20.0 Dec −17:32:25 has also been found by our photometric over-density search. It was proposed that it is at $z \sim 0.7$ in the MF sample of Olsen et al. (2007) and in the weak lensing sample of Dietrich et al. (2007).

The precise coordinates of the cluster centre (hence the BCG) are problematic to constrain. The position of the X-ray emission peak is not known exactly due to contaminating sources and because it is at the very EPIC camera's chip edge. Furthermore, all optical over-density methods have an arcmin-like spatial resolution (see dark pink contours in Fig. 4). Therefore, a tentative BCG is selected at $z = 0.71 \pm 0.07$, with the need to be confirmed by spectroscopy in the future. The tentative colour–magnitude diagram in Fig. 24 is consistent with a redshift of $z = 0.7$.

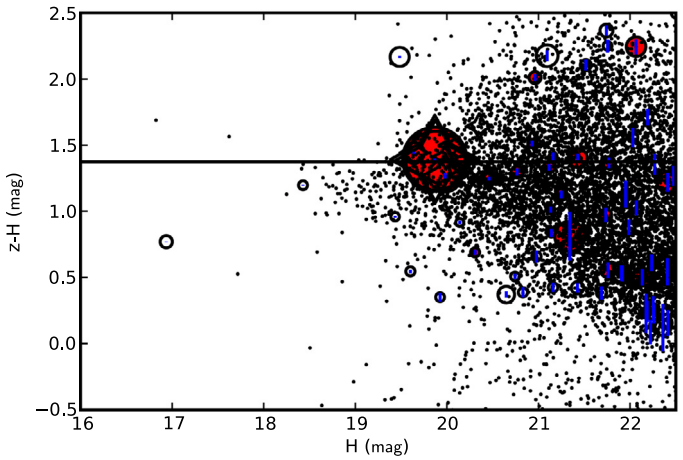

Fig. 13. As in Fig. 6a for cluster ext#4 at $z = 1.00$.

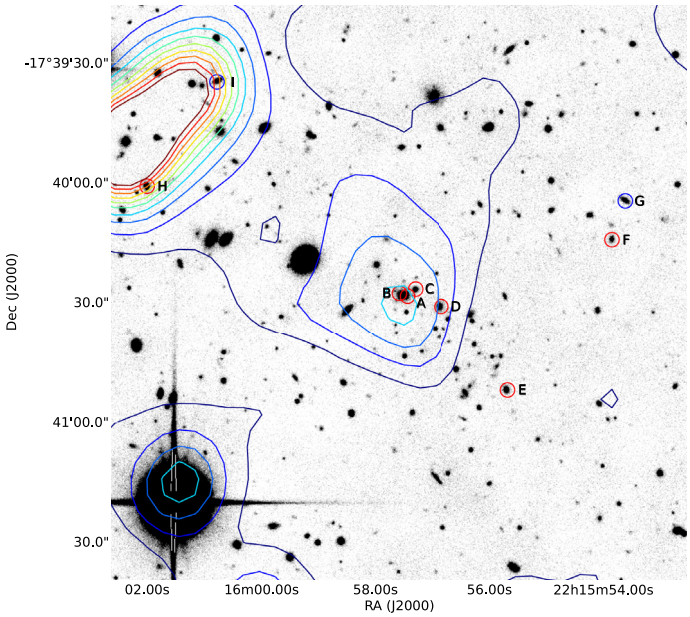

Fig. 14. As in Fig. 6b for source ext#4. The associated optical spectra are found in Fig. 15.

6. Cluster counts

6.1. X-ray sensitivity function

The advantage of using only X-rays to find clusters of galaxies is the grasp one has on the selection function. In a rather straightforward manner the X-ray behaviour of a cluster sample can be mimicked and convolved with a detector response, thereby obtaining the detection limits for various physical parameters. In this study, the survey completeness is determined using a sensitivity function, which is generated by means of Monte-Carlo simulations. The details of the simulations are presented

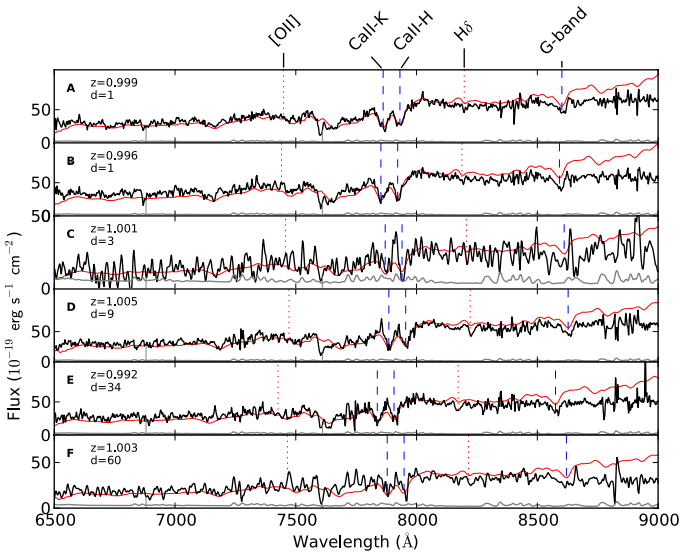

Fig. 15. Selected spectra for cluster ext#4 in the observers' frame. Colours and labels are as in Fig. 6c. Labels refer to identified objects in Fig. 14. The spectra have been smoothed.

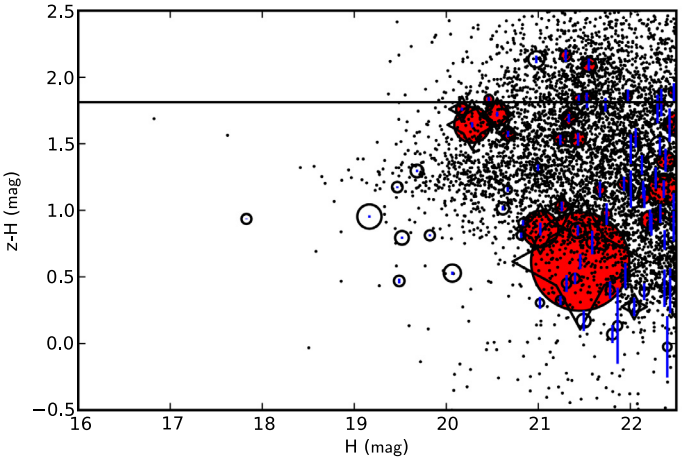

Fig. 16. As in Fig. 6a for cluster ext#5 at $z = 1.23$.

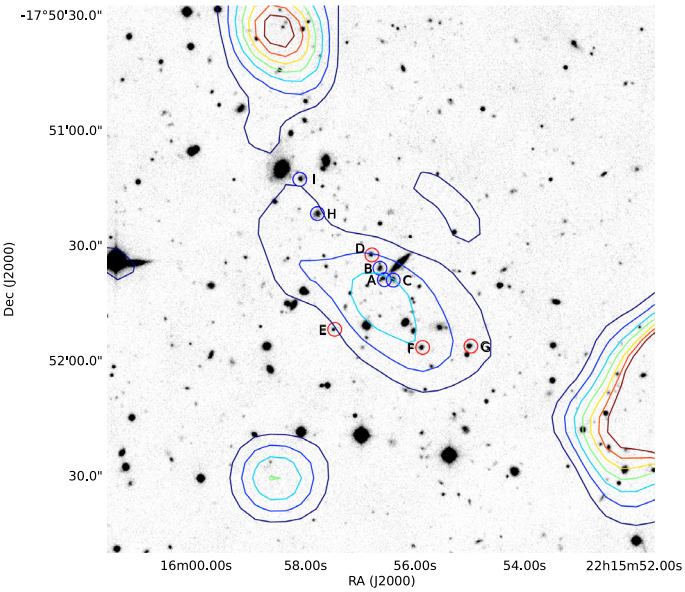

Fig. 17. As in Fig. 6b for source ext#5. The associated spectra are seen in Fig. 18.

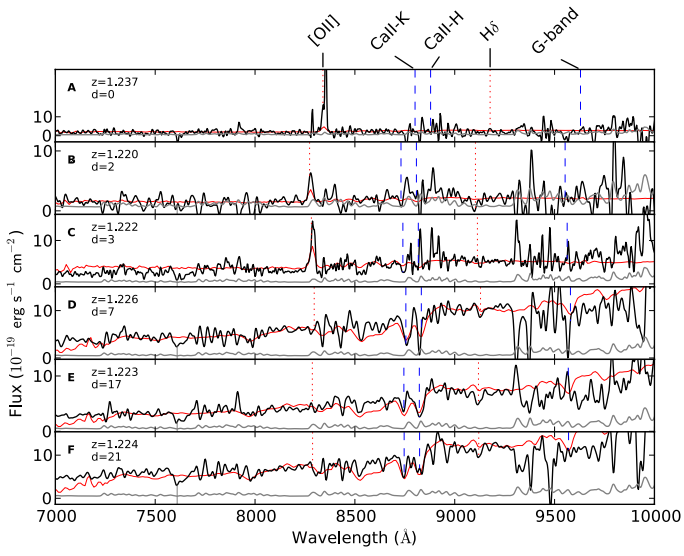

Fig. 18. Selected spectra for cluster ext#5 in the observers' frame. Colours and labels are as in Fig. 6c. The positions are seen in Fig. 17.

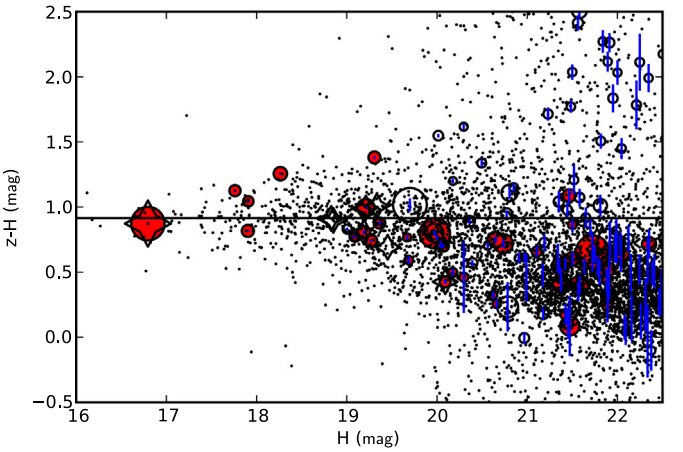

Fig. 19. As in Fig. 6a for source ext#6 at $z = 0.41$.

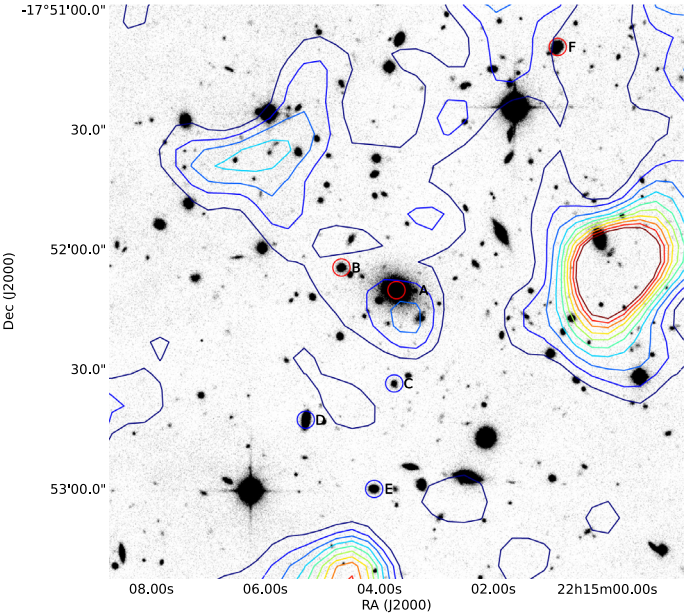

Fig. 20. As in Fig. 6b for source ext#6. The associated spectra are found in Fig. 21.

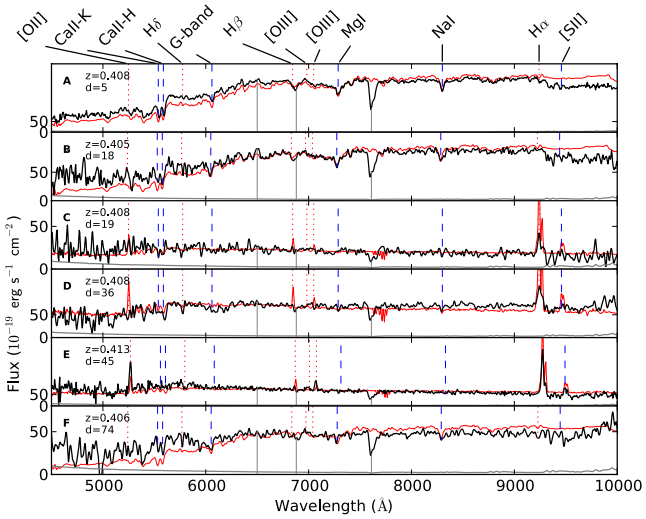

Fig. 21. Selected spectra for cluster ext#6 in the observers' frame. Colours are as in Fig. 6c. Labels refer to identified objects in Fig. 20.

in Mühlegger (2010) and discussed in Fassbender et al. (2011a). An abbreviated description is found in this section.

The probability of detecting extended X-ray sources at a (1) certain flux limit and (2) a given distance from the optical axis, is computed for ten simulated beta models ($\beta = \frac{2}{3}$) inserted randomly on concentric rings in the stacked *XMM-Newton* pointings. During insertion, regions that already contain an extended source are avoided. If this were not done, we would introduce an unphysical overlap between clusters at this faint end of the flux scale, which will result in an over-estimation of the source density when correcting for this unrealistic projection effect. The simulated clusters cover a range of 25 bins in both core radii and photon counts. This results in 3 125 simulations, since the procedure is repeated five times. The core radii distribution assumed is taken from Vikhlinin et al. (1998). The cluster sample in Vikhlinin et al. (1998) consists of 200 clusters observed with ROSAT with redshift information. The redshifts range from 0.015–0.73 with $\langle z \rangle = 0.28$. The advantage of this particular sample is that the core radius is computed by applying $\beta = 0.67$ as in our analysis. The core radii derived are scaled to how they would appear at $z = 1$ using the geometrical angular distance dependency on redshift. No further evolution is assumed. The mean core radius at $z = 1$ is ∼14 arcsec.

Source detection is performed for every simulation with `XMM-SAS v.6.5` in the multiple energy bands simultaneously with the same parameters as mentioned in Sect. 2.1. The resulting image displaying the survey completeness level as a function of limiting flux ($S_{\rm lim}$) and off-axis angle (θ) is shown in Fig. 26a. We notice that at the indicated completeness levels, the curve is rather flat between ca. 2–12 arcmin and in particular the 50% curve, which we take as the completeness level for our survey. Towards the centre of the pointing, however, an extended structure (cluster ext#1) affects the sensitivity in this observation, while on the outskirts the vignetting and the very end of the chip catastrophically affect the detectability of clusters. At the 50% level, corresponding to a flux of 2.5×10^{-15} erg cm^{-2} s^{-1}, we are complete. All clusters detected have (source detection) fluxes above this level. For our $\log N - \log S$ analysis, none of the objects ext#1-#6 needs to be excluded:

$$A(S_{\rm lim}) = \sum_{i=1}^{12} \sum_{S_{\rm lim}} A(\theta_i)\, P(\theta_i, S_{\rm lim}). \quad (10)$$

Dividing the LBQS 2212-1759 observation into rings, we can fold the geometric area with the survey sensitivity at each off-axis angle θ. We limit the radius to ≤12 arcmin. Beyond this radius the sensitivity drops significantly as seen in Fig. 26a. This area restriction also ensures the coverage by all three EPIC cameras. One extended source (ext#9) is excluded as a result of this angle limit. The cumulative effective surface area, or detection probability weighted area $A(S_{\rm lim})$, computed following Eq. (10) is displayed in Fig. 26b. Owing to our limit on the maximum radius, we obtain an survey area of ∼0.13 deg^2. $S_{\rm lim}$ denotes the limiting flux. This is the correction curve to be convolved with the clusters' number counts in the purely geometrical survey area, resulting in the survey-independent cosmological cluster count in flux bins.

6.2. $\log N$–$\log S$

The computed sensitivity function is used to predict the number of X-ray luminous clusters in a certain survey area. We convolve the probability of detecting clusters in concentric rings around the focal axis with the enclosed area (Fig. 26b). The observed flux distribution is normalised to the probability weighted survey area to obtain the expected number of galaxy clusters per flux bin. The $\log N - \log S$ graph is presented in Fig. 27. The empirical values are compared to the expected numbers simulated by Rosati et al. (2002, 1998), which in turn proved to be a good approximation for the extended X-ray source distribution in the COSMOS (Finoguenov et al. 2007) and the Subaru-*XMM-Newton* deep field (SXDF, Finoguenov et al. 2010).

When making the link between the derived flux limits and our measured fluxes, we have to bear in mind that the simulated clusters cover a range of core radii as they appear at $z = 1$. Therefore we compute S_{500} for hypothetical clusters at $z = 1$ with $r_{\rm c} = 14$ arcsec, using the iterative approach, which spans the flux range from our simulations. The mean conversion factor between $S_{\rm lim}$ and S_{500} is 0.8, which we apply to our limiting fluxes.

The intrinsic errors resulting from the method used to obtain S_{500} do not enter into Fig. 27, but only the spectral flux errors. Furthermore, since the distribution of clusters on the sky is Poissonian, we add an additional error of $\sqrt{N}$ on the number counts.

The number counts in flux bins from this study are, among others and within errors, compatible with the findings from the SXDF and COSMOS. Likewise, using spectral or source detection fluxes has no dramatic effect on the results. For low-flux objects, the scenario in which there is *no evolution* in the XLF for extended sources (Rosati et al. 2002) is favoured.

7. Summary

This work presents the detection and study of extended X-ray sources in a deep (250 ks) *XMM-Newton* field covering a FoV of ∼14 arcmin across. The nature of the sources has been identified. We have valiantly achieved "five at one blow", since this single field has allowed us to discover five new spectroscopically confirmed clusters. In the following we summarise the most essential findings from this study.

– We performed a robust source detection on deep, stacked *XMM-Newton* observations targetting LBQS 2212-1759, revealing nine extended sources with conservative detection thresholds. Six of these sources prove to be clusters of galaxies, five of which are new spectroscopically confirmed

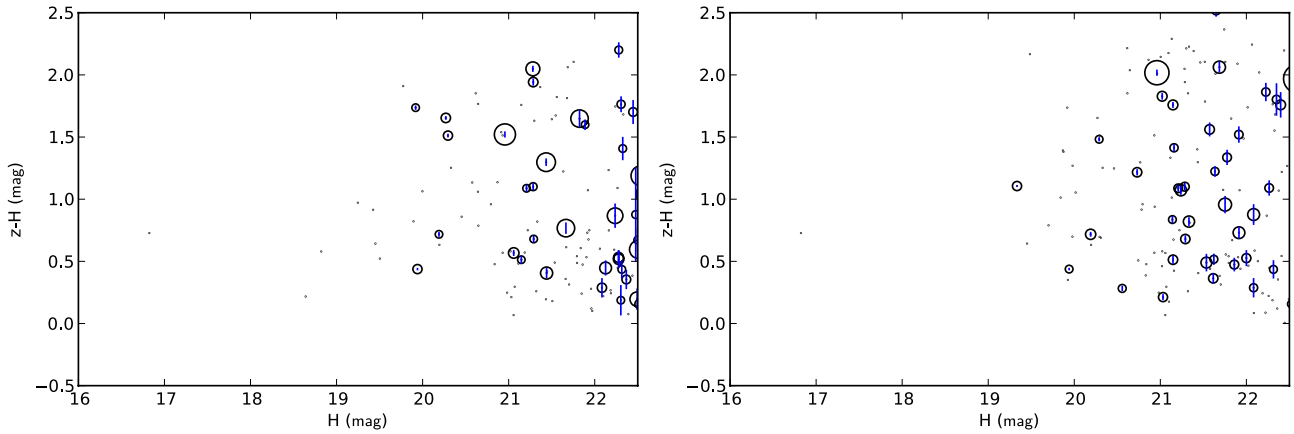

(a) Source ext#7. (b) Source ext#8.

Fig. 22. Colour magnitude diagrams around the two extended X-ray sources showing no galaxy over-density or obvious red sequence. Open circles denote all galaxies with good photometry within 1 arcmin from the X-ray centroid, scaled inversely with their distance to this centroid. Likewise, the dots represent objects within 2 arcmin.

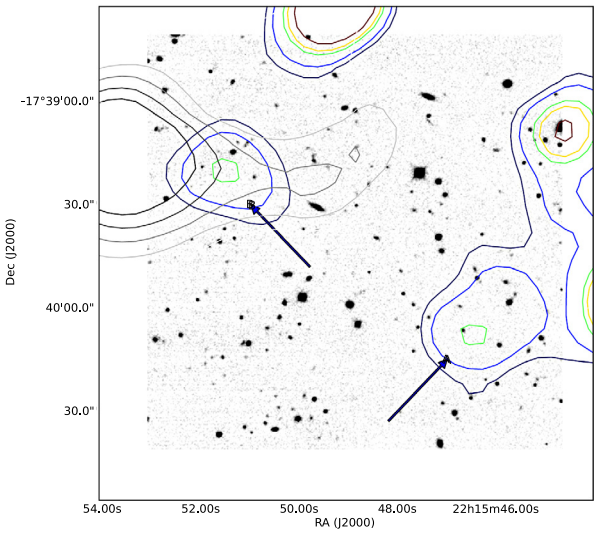

Fig. 23. Source ext#7 and source ext#8. Stack of NIR *HJK* bands to enhance depth for the two unknown structures. Source ext#8 is NW and source ext#7 SE of the image centre as pointed out by the arrows. The grey contours display the NVSS radio source. Dimension and orientation is as in Fig. 6b.

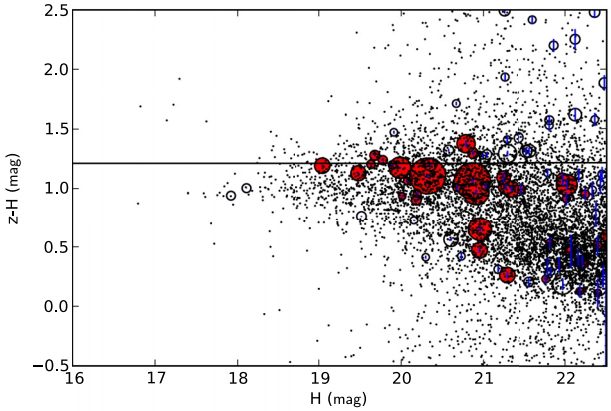

Fig. 24. As in Fig. 6a for centre coordinates as described in Sect. 5.8 close to source ext#9. The difficulty to pin-point the cluster centre results in an only vague red sequence.

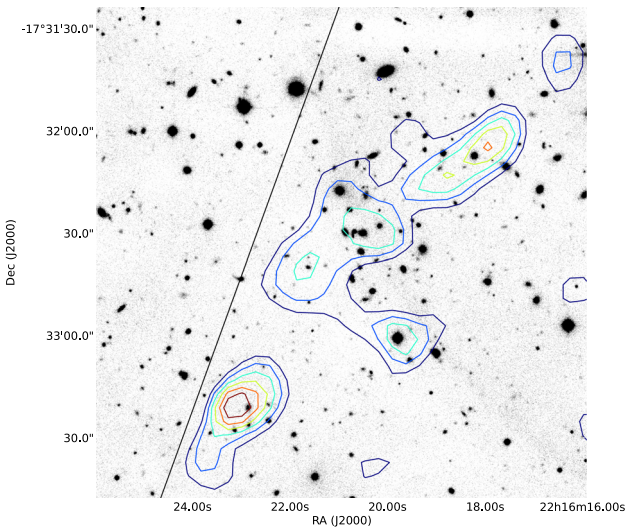

Fig. 25. As in Fig. 6b, however, the image is centred on the cluster of galaxies found close to source ext#9 (see Sect. 5.8). The extended source from our source detection is SE of the image centre. The black line indicates the end of the *XMM-Newton* EPIC chip.

discoveries from this work alone. The sixth detected cluster was already known from Stanford et al. (2006). The first unconfirmed extended source, at >14 arcmin off-axis, is a confused point source. The remaining two sources could not be identified. Since the detection of these sources is dominated by the hard energy bands, this suggests that another mechanism than bremsstrahlung is responsible for the X-ray emission from these two sources, which possibly leads at least one of them to be a Compton ghost.

– A complementary qualitative optical/IR completeness study, allowed by very deep CFHTLS data (i.e. $z'_{\rm lim} = 26.0$ $H_{\rm lim} = 24.6$), has confirmed that all X-ray luminous clusters are associated with an optical over-density, in agreement with the spectroscopic redshift. One new, significant over-density could not be correlated with any X-ray emission, hinting at a projection effect in the optical search method.
– The X-ray selection function has been computed through extensive Monte-Carlo simulations. The approach of retrieving

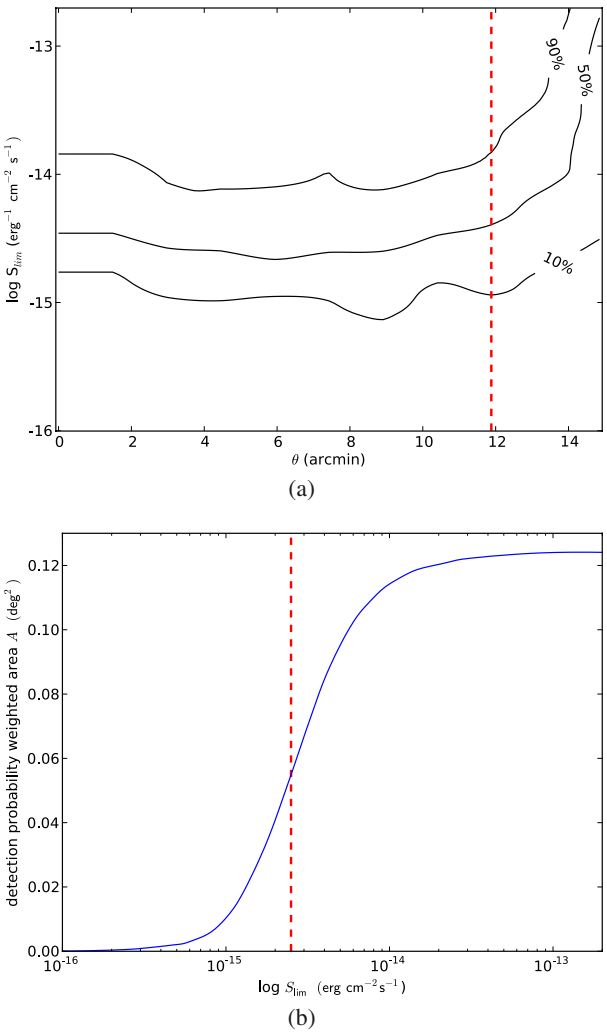

Fig. 26. a) Survey completeness as a function of off-axis angle and limiting flux. The 10%, 50% and 90% levels are indicated. The dashed red line indicates the restriction put on the off-axis angle. **b)** Cumulatively sensitivity-weighted surface areas as a function of limiting flux, integrated over all off-axis angles. The short-dashed red line indicates the deduced limiting flux of 2.5×10^{-15} erg cm^{-2} s^{-1} at which 50% completeness is reached as indicated in **a)**.

generated β models inserted into the observations has given us a 50% completeness flux limit of $\sim 2.5 \times 10^{-15}$ erg s^{-1} over most of the FoV. We constructed a $\log N - \log S$ based on a complete sample of spectroscopically confirmed sources down to weak fluxes in a precisely determined survey area with a known selection function. Our result agrees with the findings from the COSMOS and the SXDF. Comparing the number counts with the models from Rosati et al. (2002), our data seems to favour no evolution in the XLF in the faint flux range we covered.

– By spectroscopic follow-up of some X-ray point sources, we serendipitously discovered three new AGN. Two of these objects reside at the concordant redshift of the cluster (Stanford et al. 2006) at $z = 1.45$. The other quasar has a redshift of $z = 4.20$, so is among the handful of most distant X-ray-selected AGN known today (Fiore et al. 2012).

In this deep field study, good photometric data have allowed us to scan the sky in multiple wavelengths to study the galaxy counterparts of extended X-ray emission. We emphasise that photometric redshifts with errors $\Delta z < 0.1$ are still too expensive to

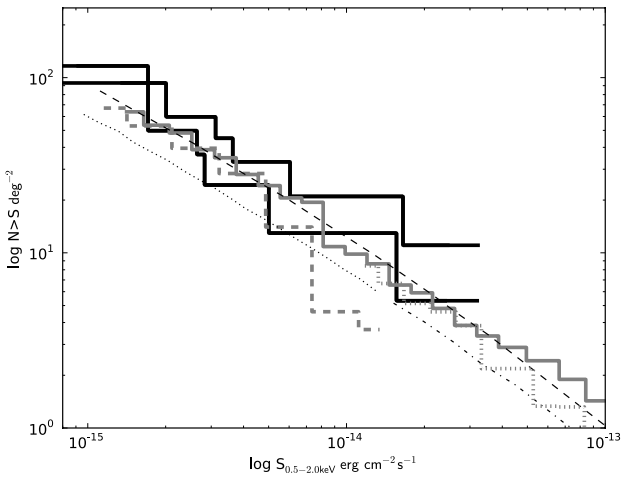

Fig. 27. Cosmological $\log N - \log S$ for clusters of galaxies. The black discrete curve shows the confidence interval resulting from measured source detection flux errors and an additional $\sqrt{N}$ on the number count from this work. A comparison to comparable surveys is made. The curves show the model from Rosati et al. (2002) for no evolution (dashed). The dot-dashed and dotted lines show the measured ROSAT brightest cluster sample (BCS, Ebeling et al. 1998) clusters and their extrapolation, respectively. The discrete lines display the findings from COSMOS (solid) (Finoguenov et al. 2007), SXDF (dashed) (Finoguenov et al. 2010), and XMM-BCS (dotted) (Šuhada et al. 2012).

date for routinely performing this kind of analysis. With respect to the upcoming X-ray mission eROSITA (Predehl et al. 2011), future optical surveys such as LSST (Ivezic et al. 2008), the ESO/Vista project VHS (Arnaboldi et al. 2007)[7], and PanStarrs (Kaiser et al. 2002) will obtain sufficient depth and cover enough area to identify a wide range of distant and faint X-ray clusters. This work, therefore, could very well be extended to a much larger area of the sky within the next decade.

In the near future, as the photometric and spectroscopic follow-up campaigns for the XDCP is becoming complete, we are already compiling catalogues of distant clusters to extend the present work.

Acknowledgements. A.d.H. was supported by the DFG under fund no. Schw536/24-2. GL acknowledges support by the Deutsches Zentrum für Luft- und Raumfahrt (DLR) under contract no. FKZ 50 OX 0201 and 50 QR 0802. J.P.D. is supported by by the German Science Foundation (DFG) through the Transregio 33 and the Cluster of Excellence "Origin and Structure of the Universe", funded by the Excellence Initiative of the Federal Government of Germany, EXC project number 153. D.P. acknowledges the kind hospitality at the MPE. This research made use of (1) APLpy, an open-source plotting package for Python hosted at `http://aplpy.github.com` and (2) IPython, an interactive python shell (Pérez & Granger 2007). We are grateful to the CFHT survey team for conducting the observations and the TERAPIX team for developing software used in this study. We acknowledge use of the Canadian Astronomy Data Centre, which is operated by the Dominion Astrophysical Observatory for the National Research Council of Canada's Herzberg Institute of Astrophysics. It is based on observations obtained with WIRCam, a joint project of CFHT,Taiwan, Korea, Canada, France, at the Canada-France-Hawaii Telescope (CFHT) which is operated by the National Research Council (NRC) of Canada, the Institute National des Sciences de l'Univers of the Centre National de la Recherche Scientifique of France, and the University of Hawaii. This work is based in part on data products produced at TERAPIX, the WIRDS (WIRcam Deep Survey) consortium, and the Canadian Astronomy Data Centre. This research was supported by a grant from the Agence Nationale de la Recherche ANR-07-BLAN-0228. This research has made use of the NASA/IPAC Extragalactic Database (NED), which is operated by the Jet Propulsion Laboratory, California Institute of Technology, under contract with the National Aeronautics and Space Administration. M.L. thanks the European Community for the Marie Curie research training network "DUEL" doctoral fellowship MRTN-CT-2006-036133.

[7] Data sharing agreement with DES (Dark Energy Survey).

Appendix A: X-ray properties and the quality of the spectral fits

In this section we present the contour plots displaying the confidence intervals of the redshift-temperature degeneracy. This method has driven the optical photometric follow-up programme.

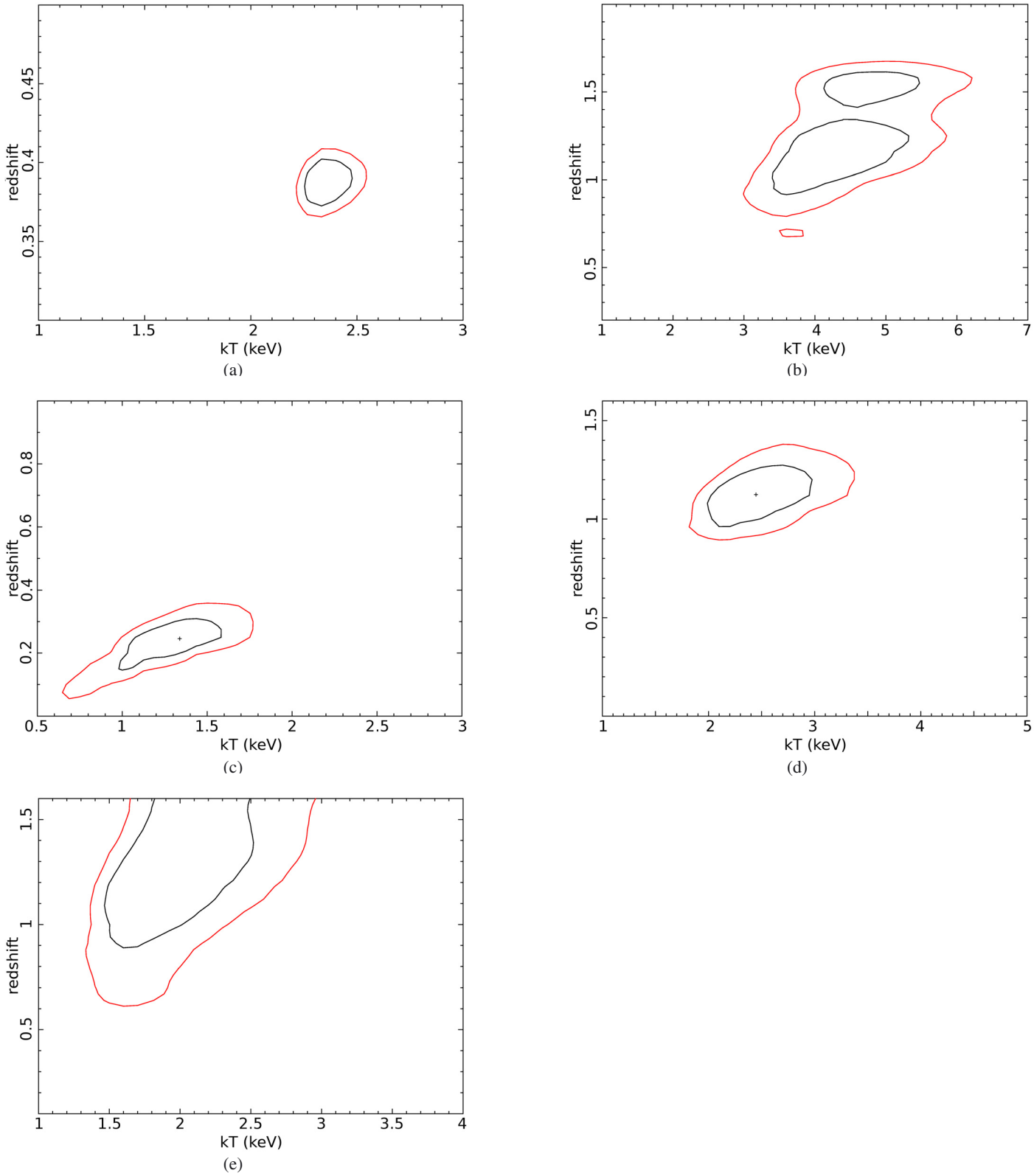

Fig. A.1. Confidence contours (68%, 90%) in redshift-temperature space for source ext#1 **a)**, source ext#2 **b)**, source ext#3 **c)**, source ext#4 **d)**, and source ext#5 **e)**.

References

Adami, C., Durret, F., Benoist, C., et al. 2010, A&A, 509, A81
Andreon, S., Maughan, B., Trinchieri, G., & Kurk, J. 2009, A&A, 507, 147
Arnaboldi, M., Neeser, M. J., Parker, L. C., et al. 2007, The Messenger, 127, 28
Bender, R., Appenzeller, I., Böhm, A., et al. 2001, in Deep Fields, eds. S. Cristiani, A. Renzini, & R. E. Williams, 96
Bertin, E., & Arnouts, S. 1996, A&AS, 117, 393
Bielby, R. M., Finoguenov, A., Tanaka, M., et al. 2010, A&A, 523, A66
Böhringer, H., Schuecker, P., Guzzo, L., et al. 2004, A&A, 425, 367
Böhringer, H., Mullis, C., Rosati, P., et al. 2005, The Messenger, 120, 33
Brimioulle, F., Lerchster, M., Seitz, S., Bender, R., & Snigula, J. 2008, unpublished [arXiv:0811.3211]
Cash, W. 1979, ApJ, 228, 939
Clavel, J., Schartel, N., & Tomas, L. 2006, A&A, 446, 439
Condon, J. J., Cotton, W. D., Greisen, E. W., et al. 1998, AJ, 115, 1693
Coupon, J., Ilbert, O., Kilbinger, M., et al. 2009, A&A, 500, 981
Dietrich, J. P., Miralles, J.-M., Olsen, L. F., et al. 2006, A&A, 449, 837
Dietrich, J. P., Erben, T., Lamer, G., et al. 2007, A&A, 470, 821
Ebeling, H., Edge, A. C., Böhringer, H., et al. 1998, MNRAS, 301, 881
Erben, T., Hildebrandt, H., Lerchster, M., et al. 2009, A&A, 493, 1197
Fabian, A. C., Chapman, S., Casey, C. M., Bauer, F., & Blundell, K. M. 2009, MNRAS, 395, L67
Fassbender, R., Böhringer, H., Nastasi, A., et al. 2011a, New J. Phys., 13, 125014
Fassbender, R., Nastasi, A., Böhringer, H., et al. 2011b, A&A, 527, L10
Finoguenov, A., Guzzo, L., Hasinger, G., et al. 2007, ApJS, 172, 182
Finoguenov, A., Watson, M. G., Tanaka, M., et al. 2010, MNRAS, 403, 2063
Fiore, F., Puccetti, S., Grazian, A., et al. 2012, A&A, 537, A16
Garilli, B., Fumana, M., Franzetti, P., et al. 2010, PASP, 122, 827
Gavazzi, R., & Soucail, G. 2007, A&A, 462, 459
Gobat, R., Daddi, E., Onodera, M., et al. 2011, A&A, 526, A133
Grove, L. F., Benoist, C., & Martel, F. 2009, A&A, 494, 845
Hayashi, M., Kodama, T., Koyama, Y., Tadaki, K.-I., & Tanaka, I. 2011, MNRAS, 415, 2670
Henry, J. P., Salvato, M., Finoguenov, A., et al. 2010, ApJ, 725, 615
Hilton, M., Stanford, S. A., Stott, J. P., et al. 2009, ApJ, 697, 436
Hilton, M., Lloyd-Davies, E., Stanford, S. A., et al. 2010, ApJ, 718, 133
Ilbert, O., Arnouts, S., McCracken, H. J., et al. 2006, A&A, 457, 841
Ivezic, Z., Tyson, J. A., Acosta, E., et al. 2008, unpublished [arXiv:0805.2366]
Kaiser, N., Aussel, H., Burke, B. E., et al. 2002, in SPIE Conf. Ser. 4836, eds. J. A. Tyson, & S. Wolff, 154
Kinney, A. L., Calzetti, D., Bohlin, R. C., et al. 1996, ApJ, 467, 38
Lamer, G., Schwope, A., Böhringer, H., et al. 2006, in The X-ray Universe 2005, ed. A. Wilson, ESA SP, 604, 729
Lamer, G., de Hoon, A., Fassbender, R., et al. 2011, in The X-ray Universe 2011, eds. J.-U. Ness, & M. Ehle, 239
Lerchster, M., Seitz, S., Brimioulle, F., et al. 2011, MNRAS, 411, 2667
Lloyd-Davies, E. J., Romer, A. K., Mehrtens, N., et al. 2011, MNRAS, 418, 14
Mignano, A., Miralles, J.-M., da Costa, L., et al. 2007, A&A, 462, 553
Mühlegger, M. 2010, Ph.D. Thesis, Technischen Universität München
Mullis, C. R., Rosati, P., Lamer, G., et al. 2005, ApJ, 623, L85
Nastasi, A., Fassbender, R., Böhringer, H., et al. 2011, A&A, 532, L6
Olsen, L. F., Benoist, C., Cappi, A., et al. 2007, A&A, 461, 81
Papovich, C., Momcheva, I., Willmer, C. N. A., et al. 2010, ApJ, 716, 1503
Pérez, F., & Granger, B. E. 2007, Comput. Sci. Eng., 9, 21
Pierre, M., Clerc, N., Maughan, B., et al. 2012, A&A, 540, A4
Postman, M., Lubin, L. M., Gunn, J. E., et al. 1996, AJ, 111, 615
Predehl, P., Andritschke, R., Becker, W., et al. 2011, in SPIE Conf. Ser., 8145
Reichert, A., Böhringer, H., Fassbender, R., & Mühlegger, M. 2011, A&A, 535, A4
Rosati, P., della Ceca, R., Norman, C., & Giacconi, R. 1998, ApJ, 492, L21
Rosati, P., Borgani, S., & Norman, C. 2002, ARA&A, 40, 539
Santos, J. S., Fassbender, R., Nastasi, A., et al. 2011, A&A, 531, L15
Schwope, A. D., Lamer, G., Burke, D., et al. 2004, Adv. Space Res., 34, 2604
Stanford, S. A., Romer, A. K., Sabirli, K., et al. 2006, ApJ, 646, L13
Stanford, S. A., Brodwin, M., Gonzalez, A. H., et al. 2012, ApJ, 753, 164
Takey, A., Schwope, A., & Lamer, G. 2011, A&A, 534, A120
Tanaka, M., Finoguenov, A., & Ueda, Y. 2010, ApJ, 716, L152
Šuhada, R., Song, J., Böhringer, H., et al. 2012, A&A, 537, A39
Vikhlinin, A., McNamara, B. R., Forman, W., et al. 1998, ApJ, 502, 558
Vikhlinin, A., Burenin, R. A., Ebeling, H., et al. 2009, ApJ, 692, 1033
Watson, M. G., Schröder, A. C., Fyfe, D., et al. 2009, A&A, 493, 339